Fibrous Materials for Flexible Li-S Battery

Yuan Gao, Qianyi Guo, Qiang Zhang, Yi Cui, and Zijian Zheng*

Dr. Y. Gao, Q. Guo, Prof. Z. Zheng

Laboratory for Advanced Interfacial Materials and Devices, Research Centre for Smart Wearable Technology, Institute of Textiles and Clothing, The Hong Kong Polytechnic University, Hong Kong SAR, China.

Prof. Z. Zheng

Research Institute for Smart Energy, The Hong Kong Polytechnic University, Hong Kong SAR, China.

E-mail: tczzheng@polyu.edu.hk

Prof. Q. Zhang

Beijing Key Laboratory of Green Chemical Reaction Engineering and Technology, Department of Chemical Engineering, Tsinghua University, Beijing 100084, China.

Prof. Y. Cui

Department of Materials Science and Engineering, Stanford University, Stanford, CA 94305, USA.

Prof. Y. Cui

Stanford Institute for Materials and Energy Science, SLAC National Accelerator Laboratory, 2575 Sand Hill Road, Menlo Park, CA 94025, USA.

Abstract: Lithium-sulfur (Li-S) battery is an attractive high-energy-density technology to power future flexible and wearable electronics. The challenge is how to simultaneously achieve adequate flexibility, stability, and energy density to the Li-S battery system. Recent studies show that fibrous materials are promising to achieve flexible batteries with high energy density, by taking advantages of their intrinsic flexibility, lightweight, large surface area, and cost-effectiveness. Fibrous materials are structurally and functionally diverse to construct various components of a working battery, including current collectors, buffer layers, interlayers, and solid-state electrolytes. This review summarizes the recent development of fibrous materials for flexible Li-S batteries, with an emphasis on the discussion of the synthesis and preparation of materials, design of fibrous structures and functionalities, and layout of battery cells for achieving high Coulombic efficiency, long cycle life, and good flexibility.

1. Introduction

The realization of advanced functions of flexible and wearable electronics, such as smart textiles,[1] implanted/epidermal monitors,[2-4] and rolled-up touch screens,[5] requires the seamless build-in of batteries into these soft products. Therefore, it is highly desirable to fabricate batteries with both high energy density and good flexibility.[6-10] Among various battery technologies, lithium-sulfur (Li-S) batteries have received considerable attention due to their ultrahigh theoretical energy density (2567 W h kg^{-1}), environmental benignancy, and low cost of S.[11-13] However, their applications in the wearable electronics are hampered by the severe interfacial issues, *e.g.,* the formation of Li dendrites and the shuttle effect of polysulfide, which occur in the Li-S chemistries.[14-18] In addition, most Li-S batteries exhibit poor mechanical stability and low areal capacity.[11, 12, 18]

During the past decades, there is an increasing interest in the development of cutting-edge materials that can simultaneously endow Li-S batteries with high energy, long cycle life, and good flexibility.[11, 18, 19] Among those, fibrous materials represent a promising option attributing to their large surface area (10^{2-3} m^2 kg^{-1}), lightweight, good flexibility, and cost-effectiveness. Generally, fibrous materials are in the form of high-aspect-ratio (>50) fibers, filaments, yarns, and their superstructures with the geometrical sizes from several hundreds of nm to m.[20] Material wise, they consist of metals, carbons, ceramics, polymers, and composites of those.[21-25] The fibrous materials provide a solid, hollow, core-shell, or hierarchically porous structure.[26-30] Mechanically, most of the fibrous materials are flexible and even stretchable, which can sustain complex deformations.[31-33] Technically, fibrous materials and their assemblies are highly manufacturable via various high-throughput methods such as spinning, vacuum infiltration, and textile technology.[34-36] With these appealing properties, fibrous materials have been demonstrated to serve as different battery components of Li-S batteries

3

(Figure 1), including current collectors of both Li anodes and S cathodes, buffer layers, interlayers, and solid-state electrolytes (SSEs).

Considering the great promises of utilizing fibrous materials in Li-S batteries, this review presents the recent advances of this rapidly developing area. We firstly introduce the working principles and the challenges of Li-S batteries (Section 2). We then give an overview of the advantages of using fibrous materials for flexible Li-S batteries (Section 3). After that, we provide an in-depth discussion on the preparation of fibrous materials and the design of fibrous structures and functionalities for flexible current collectors (Section 4) and flexible interfacial layers (Section 5) of Li-S batteries, with a special focus on the enhancements of electrochemical and mechanical performances of Li anodes and S cathodes. Regarding the device-level performance, we finally highlight several layouts of flexible Li-S batteries including wire-type battery, battery with integrated architecture, and foldable battery (Section 6).
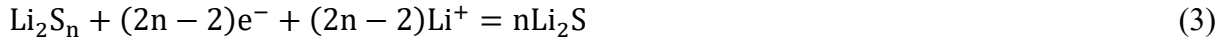
2. Working principle and challenges of Li-S batteries

Li-S batteries release energy via conversion reactions between the Li metal anode and S cathode. Li metal is oxidized to produce Li^+ and electrons at the anode, which travels through the electrolyte and external circuit respectively to the S cathode. At the cathode side, there is a two-step discharging process. Initially, the cyclo-S_8 is reduced to long-chain polysulfides (Li_2S_n, $4 \leq n \leq 8$) at the voltage plateau $\approx 2.3V$. After that, these soluble polysulfides dissolve in the electrolyte, following with the precipitation in the form of solid Li_2S_2/Li_2S at $\approx 2.1V$.[13] The above discharging process is described with the equations below.

For the Li anode:

$$2Li = 2Li^+ + 2e^- \tag{1}$$

For the S cathode:

$$\left(\tfrac{n}{8}\right) S_8 + 2e^- + 2Li^+ = Li_2S_n (4 \leq n \leq 8) \tag{2}$$

$$Li_2S_n + (2n-2)e^- + (2n-2)Li^+ = nLi_2S \tag{3}$$

The electrochemical Li-S chemistries during the charge/discharge are listed in Figure 2. a) The formation of SEI on Li metal anode tends to dry out the electrolyte, which leads to the low Coulombic efficiency (CE) and short cycling lifespan of the Li anode. Additionally, the as-obtained Li dendrites can penetrate the separator and shortly connect the anode and cathode, raising the thermal runaway of the battery.[15] b) The dissolution and migration of soluble Li_2S_n (n ≥4) in the organic electrolyte lead to an irreversible loss of S resource. c) The electrically insulating nature of S/Li_2S results in the low utilization of cathodes and sluggish kinetics of redox reactions. d) The huge volumetric change due to electrochemically conversion among different S species causes the pulverization and detachment of cathodic materials from the current collector, thus posing a rapid capacity decay of the S cathode.[37, 38]

Besides the electrochemical issues mentioned above, Li-S batteries also face the following mechanical challenges in flexible applications. i) Current collectors of Li-S batteries are in the form of thin metal foils of Cu (Li anode) and Al (S cathode). These metal foils crack and fracture after being repeatedly bent to a small radius of curvature (<10 mm) because of their intrinsically low yield strains (Cu, 1.2 %; Al, 0.9 %).[39-41] The severe incompatibility between rigid metal foils and other soft battery components causes displacement among each battery component upon flexing the battery.[11] ii) Because of the same reason, although Li foil is very soft, it also undergoes permanent distortion (crack or fracture) after multiple flexures.[42, 43]

Concerning the wearable aspect, the liquid electrolyte is flammable and takes a risk of leakage, which poses a safety issue in the wearable devices.[44]

3. Advantages of fibrous materials for flexible Li-S batteries

The applications of fibrous materials and structures in flexible Li-S batteries presents multi-fold advantages as shown in Figure 3. Electrochemically, fibrous Li anode and S cathode can achieve higher capacities than those of thin-film electrodes because of the large electrically interfacial contact between the fibrous current collectors and respective active materials.[45] Moreover, fibrous current collectors and interfacial layers can relieve the parasitic reactions of Li-S batteries through various tactics, including 1) reduction of localized current density, navigation of Li deposition, redistribution of Li$^+$ flux, and stabilization of SEI at the Li anodes; 2) acceleration of reaction kinetics by electrocatalysts, accommodation of volumetric change, suppression of shuttle effect at the S cathodes. Mechanically, fibrous materials are highly flexible and fatigue-resistant, which is favorable in flexible applications. Fibrous Li anodes exhibit better mechanical stability than Li foils, benefiting from their structural reinforcement by fibrous materials. Taking the above advantages, fibrous materials enable the assembly of high-energy, long cycle life, and flexible Li-S batteries with various formats, including wire-type batteries, batteries with integrated architecture, and foldable batteries. The following sections will discuss the details of using fibrous materials for different parts of the flexible Li-S batteries including current collectors, buffer layers, interlayers, and SSEs, and how they improve the energy density, stability, and flexibility of the Li-S cells.

4. Flexible current collectors

Electrically conductive fibrous materials can work as current collectors for both Li anode and S cathode. This section describes the frequently used materials and fabrication technologies for the preparation of fibrous current collectors. It also discusses the enhancements of electrochemical performance and mechanical performance of Li anodes and S cathodes with the use of fibrous current collectors.

4.1 Fibrous carbons

Fibrous carbons mainly consist of carbon nanotubes (CNTs), carbon nanofibers (CNFs), carbonized fibers, and their hybrids (CNTs/graphene, CNFs/rGO) and superstructures (woven/nonwoven carbon fabrics (CFs)). Methods including chemical vapor deposition (CVD), spinning (dry/wet spinning, electrospinning), vacuum filtration, and carbonization are frequently reported for controllable synthesis of fibrous carbons.[22, 46-52] Among those, CVD represents a facile technology for the preparation of CNTs with various morphologies such as multi-walled CNTs (MWCNTs), vertically aligned CNTs (VACNTs), super-aligned carbon nanotube (SACNTs) and tube-in-tube CNTs.[22, 52-54] A recent study successfully used CVD-grown CNTs as the flexible and self-supported current collectors of S cathodes (Figure 4a and b). The S-CNTs cathode exhibited a good flexibility (able to withstand a 10 MPa stress) and remarkable fatigue durability (8.0 S cm^{-1} after 12000 flexure). It also attained a high discharge capacity of 712 mAh g^{-1} (23 wt % of S) and 520 mAh g^{-1} (50 wt% of S) at a high current density (6 Ag^{-1}).[55]

4.2 Fibrous metals

One-dimensional nanostructures of metals, *e.g.*, nanowires, nanotubes, nanorods, etc. are particularly attractive for current collectors of energy storage devices due to their high electrical conductivity. These materials are commonly achieved via the process of template-assisted vapor deposition (chemical vapor deposition (CVD), sputtering, evaporation), hydrothermal conversion, and electrochemical deposition (ED).[27-29, 56] In comparison to metal nanowires, micro-sized metal filaments and meshes possess the advantages of more mature fabrication technology, lower prices, and better mechanical robustness, which can realize scalable preparation of fibrous Li anodes or S cathodes. For instance, a 30 cm fiber-shaped S cathode

can be synthesized via a simple capillary infusion of S particles into a bundle of stainless steel filaments, while a fibrous Li anode was achieved after one-step pressing of Li foils into the Cu mesh (Figure 4c and d).[24, 57] However, these micro-sized fibrous metals are heavy and thick (*e.g.* 100 μm Cu mesh: 20 mg cm^{-2}). Such a drawback shall deteriorate the flexibility and energy density of the batteries.

4.3 Fibrous metallic composites

Fibrous metallic composite generally consists of a core-shell architecture with highly compliant non-metal fibers (*e.g.* carbonaceous fibers or polymer fibers) as the core and metal nanoparticles/thin films as the shell. Electrochemical deposition and electroless deposition are the most adopted methods to coat metallic layers on the surfaces of conductive and non-conductive fibers, respectively. Fibrous metallic composites can display high electrical conductivity and desirable flexibility. For instance, a Ni-coated polyester textile prepared by electroless plating achieved a low sheet resistance of 0.35 Ω sq^{-1}, of which the value was several orders of magnitude smaller than those of fibrous carbons. Additionally, such a metallic textile remained mechanically robust after 100 cycles folding/unfolding.[58] One key challenge of this material is poor adhesion of the metallic layer on the polymer core. To tackle this problem, a polymer-assisted metal deposition (PAMD) method to fabricate highly flexible and conductive fibrous metallic composites was developed.[59, 60] In PAMD, a functional polymer layer was grafted on the surface of the polymer fiber core and acted as a medium for firmly tethering the metallic layer onto the fiber surface (Figure 4e and f). This interlayer improved the electrical conductivity without affecting the flexibility, and endowed fibrous metallic composites with excellent fatigue resistance during repeated flexing. For instance, the Ni-coated cotton yarns displayed a low linear resistance of 1.3 Ω cm^{-1}, and such a value remained unchanged over 5000 bending cycles at a bending radius of 1 mm (Figure 4g).[21]

4.4 Current collectors of Li anodes

4.4.1 Reduction of localized current density and navigation of Li deposition

The uneven distribution of spatial charge at the surface of Li metal accounts for the formation of Li dendrites. During such a process, Li initially reacts with organic solvents and Li salts in the electrolyte to form fragile SEI, which usually results in uneven thickness due to the concentration variation of localized Li$^+$. The large volumetric change associated with the hostless plating of Li then breaks the SEI and exposure of fresh Li metal to the electrolyte. With further deposition, Li metal underneath a cracked SEI or thin SEI grows faster than the intact or thick SEI counterpart. The growth of Li is accelerated with the increase of current densities, which finally causes the formation of Li dendrites.[61] Sand's time model describes the initial nucleation of Li dendrites:[62]

$$\tau = \frac{\pi D}{4}\left(\frac{z_c C_0 F}{J t_a}\right)^2 \tag{4}$$

where the Sand's time τ indicates the time for the concentration of Li$^+$ at the surface of Li dropping to zero and the dendritic Li starting to grow, D is the ambipolar diffusion coefficient, z_c is the charge number of the cation (z_c=1 for Li$^+$), F is the Faraday's constant, J is the effective electrode current density, t_a is the anionic transference number, C_0 is the initial concentration of Li$^+$.

Fibrous current collectors commonly have large electrochemically active surface area. They can relieve the formation of Li dendrites through the reduction of localized current densities (*J*) and the navigation of Li deposition. Liu et al. proposed a 3D hollow CNF (3D-HCNF) as the container for the storage of Li at a high areal capacity.[63] The 3D-HCNF initially confined the growth of Li inside the hollow tubular fibers, and further guided the deposition of Li within the interspace among neighboring fibers (Figure 5a and b). Such a unique architecture also provided

a high electroactive surface area, which can significantly reduce the localized current density. As such, 3D-HCNF-based Li anode achieved a high areal capacity of 6 mAh cm^{-2}, a high CE of 99.5 %, and a long lifespan over 1200 h.

Fibrous carbons with different architectures such as CNF networks,[64] carbon nanotube (CNT) sponges,[65, 66] CNT decorated graphite composites[67] were also reported as flexible and dendrite-free current collectors of Li anodes. A major hurdle of fibrous carbon is their higher sheet resistance (1 Ω sq^{-1} with maximum percolation) in comparison to that of metals (10 μm Cu foil: 1.6×10^{-3} Ω sq^{-1}), which poses battery a high ohmic loss.[68] To address such an issue, Lu et al. adopted a cost-effective solution process to fabricate a Cu nanowire-based Li anode, which displayed a high electrical conductivity with an areal resistance below 2×10^{-2} Ω cm^{-2} and a high areal capacity (7.5 mAh cm^{-2}).[69] The large surface area of Cu nanowires offered a large Li/electrolyte interface for the fast transportation of electrons (Figure 5c). Consequently, flexible Li anode achieved a low voltage hysteresis of 40 mV (Figure 5d) and a stable CE of 98.6 % for 200 cycles. Since fibrous metals favor Li anode to achieve a low voltage hysteresis, 3D Cu decorated with the fibrous submicron skeleton[70] and 3D pie-like Cu nanowires,[71] were later proposed for fibrous Li-S batteries.

Methods including ED, evaporation, roll-pressed, and molten infusion of Li have been reported for preparation of fibrous Li anodes.[42, 66, 72, 73] Among those, ED is a dominant technology because it can deposit Li with controllable morphologies. In a recent work, a certain amount of Li (6 mAh cm^{-2}) was conformally coated on the surface of a fibrous metallic composite, namely Cu-coated CF (CuCF), to yield the Li/CuCF anode (Figure 6a).[74] The as-deposited Li nanoflakes uniformly distributed on each Cu-coated C fiber (Figure 6b). The CuCF efficiently stabilized the long-term stripping and plating of Li by reducing the nucleation and mass-transfer overpotentials of Li, while the well retained Li nanoflakes provided a fast

transport of Li^{+}. These advantages enabled Li/CuCF anode to stably run for more than 500 h with a low overpotential of ≈20 mV (Figure 6c) and achieve an extremely high CE of >99.89 %.

The infusion of molten Li into fibrous current collectors is regarded as a scalable and fast process for fabricating fibrous Li anodes.[75-77] Materials including metals,[76] inorganic non-metals,[78] metal oxides,[73, 77] and specialized functional groups[75, 79] can enhance the lithophilicity of the fibrous current collectors by spontaneously reacting with molten Li. Recently, Niu et al. reported an amine-decorated mesoporous CNFs for the infusion of molten Li.[75] The -NH groups altered the surface of CNFs from non-wetting to wetting with Li, thus the molten Li can quickly infiltrate the carbon film and fill the pores/cavities of CNFs (Figure 6d). The Density Functional Theory (DFT) calculation further confirmed that the Li tended to nucleate and grow into the form of clusters around -NH groups because of the thermodynamically favorable binding of Li atoms with -NH groups (Figure 6e). It facilitated the uniform deposition of Li along the axial direction of the CNFs during plating and stripping for 200 cycles' test. The deposition of Li on the surface of non-treated CNFs, however, exhibited a vertical direction of growth, which led to the formation of Li dendrites after only 10 cycles (Figure 6f and g).

4.4.2. Improvement of flexibility/stretchability of Li anodes

Li can easily undergo plastic deformation because of its low yield strain (~0.4%). The use of fibrous current collectors can enhance the mechanical stability of Li anodes.[42, 43] A flexible Li anode (55 μm) was fabricated via a simple roll-pressing of Li foil into a Ni- and Cu-plated conductive poly(ethylene terephthalate) nonwoven at room temperature (Figure 7a).[42] The reinforced Li metal was bendable (Figure 7b) and could wind around a rod without any mechanical rupture (Figure 7c). The good mechanical stability of the anode was further verified by measuring the variation of the resistance during multiple longitudinal compression. The Li

metal composite well retained its structural integrity and presented a marginal change of resistance after 110,000 bending cycles. The pristine Li metal, however, showed a drastic increase of resistance after less than 700 bending cycles because of the fracture of Li (Figure 7d).

To adapt to the complicated motion and mate the epidermal surface of the human body, wearable batteries are expected to possess not merely good flexibility but also certain stretchability. For the first time, Liu et al. successfully used doubly coiled Cu wire embedded rubber as a monolithic stretchable current collector of Li metal anode. The whole electrode consisted of patterned Li metal microdomains connected by highly elastic rubbers (Figure 7e). Upon stretching, the rubber can efficiently absorb the mechanical strain while the Li domains were not affected. Such a unique "one-body" configuration efficiently alleviated the modulus differences between polymer and lithium. Consequently, the lithium anode under 60 % strain exhibited a stable CE of ≈95 % for 30 cycles (Figure 7f).[31]

4.5 Current collectors of S cathodes

4.5.1 Enhancement of electrical conductivity of S/Li$_2$S

Cathodic materials such as S and Li$_2$S typically show low electrical conductivity. Constructing fibrous current collectors with hierarchical architectures can solve this problem. So far, CNTs,[80] CNFs,[81, 82] graphene-based network,[83] carbonized fibers/fabric[84] and their hybrids[85] were broadly reported as good flexible S/Li$_2$S current collectors. For example, Yuan et al. developed a CNT-based current collector (7.1 S cm^{-1}) consisting of highly conductive multi-walled CNTs (MWCNTs) and mechanically robust vertically aligned CNTs (VACNTs) (Figure 8a).[86] MWCNTs, 15 nm in diameter and 10-50 μm in length, served as the short-range electrically conductive pathway, while super long VACNTs, 50 nm in diameter and 1-2 mm in length, worked as both a long-range conductive network and intercrossed mechanical scaffold

(Figure 8b). Such a hierarchical structure provided an omnidirectionally electrical pathway, which favored flexible S cathode to achieve a high initial discharge capacity of 995 mAh g^{-1}, and a low capacity decay (0.20 % per cycle) within 150 cycles (Figure 8c). The interlinked structure without use of metal foils as the current collectors also enabled the stacking of the cathodes for achieving high areal capacities. For instance, the areal capacities of the single-, double-, and triple-layer cathodes were 6.2, 9.4, and 15.1 mAh cm^{-2} @0.05 C, respectively (Figure 8d). Other hybrid materials such as aligned CNT/mesoporous carbon (CMK-3),[87] CNT/graphene oxide (GO)/CMK-3,[88] CNT/reduced graphene oxide (rGO),[89] and rGO-coated porous CNF[90] have also been used as flexible current collectors for the enhancement of electrical conductivity of S/Li$_2$S.

Incorporation of S/Li$_2$S particles into the porous current collectors is another effective tactic to enhance their electrical conductivity. Sun et al. prepared mesoporous super aligned CNTs (SACNTs) via an ambient thermal oxidation (550°C) process.[91] Abundant mesopores served as adsorption points to electrically wrap the insulating S particles (Figure 8e), which achieved a higher electrical conductivity (58.0 S cm^{-1}) than the pristine cathode (35.0 S cm^{-1}). S @SACNTs achieved a high initial (1264 mAh g^{-1}) and reversible capacity (866 mAh g^{-1} at 100th cycle @0.1C), and good rate performance (Figure 8f). Since then, magnesium oxide and nanosized silica were synthesized as sacrificial templates to fabricate porous current collectors.[92, 93]

4.5.2 Anchor of soluble polysulfides

During the charging process, the highly soluble intermediates Li$_2$S$_n$ (n ≥ 4) easily diffuse to the Li anode. It causes the self-discharge of battery and the loss of S species, known as the shuttle of polysulfides. The physical or chemical anchor of soluble polysulfides on the cathodic current

collectors can suppress the shuttle effect, which is favorable for the S cathodes to achieve a high specific capacity.

Current collectors with micropores are superior to those of mesopores and macropores in stabilizing the cycling performance of Li-S batteries because of their strong capillary force for the effective anchor of soluble polysulfides. However, a high value of Li^+ transference is likely to achieve from macroporous current collectors because of the unrestricted diffusion pathway of Li^+. In this scenario, the design of current collectors with hierarchical pores benefits the simultaneous realization of fast transport of Li^+, high rate performance, and good cycling stability.[94] Zhao et al. demonstrated a hierarchically porous CNF (HPCNF) with a centered macropore (>100 nm) enveloped by a denser cycle of micro/mesopores (1.8 and 4.1 nm) on the periphery (Figure 9a).[95] The small-size pores provided a strong capillary force to immobilize the soluble polysulfides, while the large pores promoted the diffusion of Li^+. The as-fabricated S cathode achieved high initial capacities of 1460, 1394, 1352, and 1316 mAh g^{-1} @0.05 C with different mass loading of 2.2, 4.8, 6.1, and 8.3 mg cm^{-2}, respectively, and good rate performance (Figure 9b).

A drawback of physical confinement lies in its weak van der Waals force between the nonpolar fibrous hosts and polar polysulfides. Especially for a battery undergoing a fast charging/discharging process, the attractive force is too weak to restrain the dissolution of soluble polysulfides. In contrast, chemical confinement can provide a stronger interfacial interaction between current collectors and S species than that of physical confinement.[96] Typical chemical confinement includes chemical affinity and chemical bonding. The chemical affinity refers to polar-polar interactions between polar compounds on the surface of fibrous current collectors and polysulfides. The lithium bonds originate from the electron-rich donors (*e.g.*, pyridinic nitrogen) and Li polysulfides via Li, which is enhanced by the inductive and conjugative effect of hosts, which is an emerging interaction in a working Li-S battery.[97] The

chemical bonding forms during the chemical reaction between polysulfides and the special functional groups, atoms, and molecules on the fibrous matrix. In practice, chemical and physical confinements are frequently used together to supply a synergistic restriction of diffusion of polysulfides.

Metal compounds including metal oxides (*e.g.*, TiO_2,[98] MnO_2,[99] Fe_3O_4,[100] and perovskites[101]), metal sulfides (*e.g.*, MoS_2,[102, 103], CoS,[104] CoS_2,[105] and Co_9S_8[106, 107]), metal selenide (*e.g.*, $CoSe_2$[108, 109]), and metal nitride (*e.g.*, VN[110]) provide good chemical affinity to polysulfides due to their strong polar metal/non-metal bonding. Therefore, they are usually decorated on the fibrous current collectors to serve as absorbents of polysulfides.[104, 111-116] Zhong et al. reported a S scaffold by compositing the VN nanobelt arrays with porous carbon (PCF/VN) (Figure 9c).[110] The binding energy between polysulfides and the VN nanobelt arrays was 3.75 eV, showing a much larger value than that of bare carbon (1.07 eV). The high binding energy suggested a strong chemisorption of soluble polysulfides, which favored the composite cathode (PCF/VN/S) to simultaneously achieve a high initial discharge capacity of 1310.8 mAh g^{-1} and a high areal capacity of 10 mAh cm^{-2} @0.1 C. It further endowed the PCF/VN/S cathode with a high capacity retention of 80.3 % after 250 cycles. The electrochemical performances of PCF/VN/S greatly outperformed that of CF/VN/S, PCF/S, and CF/S cathodes (Figure 9d).

Metals can also form chemical bonds with S species.[117] The examples include Cu-stabilized CNFs,[118] Ni-coated CFs,[74, 119] and bimetallic CoNi nanoparticle embedded CNFs.[120] In a recent work, a Ni-coated carbon fabric (NiCF) exhibited favorable interaction with S species by not only forming a strong chemical bond of Ni-S, but also providing catalytic function to promote the conversion reaction among different S species (Figure 9e).[74] The DFT calculation showed that the Ni (111) possessed a larger adsorption energy of -3.51 eV and a smaller decomposition energy of 0.2 eV for Li_2S than that of rGO, N-doped graphene (NGr), and N, S-

doped graphene (NSHG), suggesting a rapid oxidation of Li_2S back to S with the use of NiCF current collector (Figure 9f). The high catalytic activity of NiCF enabled a high capacity retention of S cathode (99.82% per cycle) over 400 cycles with a S loading of 2.4 mg cm^{-2}, tested @0.5 C (Figure 9g). When pairing such a cathode (3 mAh cm^{-2}) with the Li anode (6 mAh cm^{-2}), the Li-S battery obtained a high cell energy density of 360 Wh L^{-1} and 288 Wh kg^{-1}, and showed an excellent cycling stability of 260 cycles (Figure 9h).

Oxygen functional groups (-OH, -COOH) and PEDOT/PSS can also immobilize soluble polysulfides by forming strong -S-O- bond.[121] The heteroatom doping is another approach to strengthen the chemical bonds between current collectors and polysulfides. For illustration, the introduction of the nitrogen atom in the fibrous carbons provides two types of attraction for the anchor of soluble polysulfides, including 1) the attraction between Li^+ in polysulfides and pyridinic nitrogen dopants, 2) the attraction between Li^+ captured by pyridinic nitrogen dopants and S anions.[94, 122] Recently, incorporation of few-layer nanosheets of phosphorene has displayed significant enhancement on the immobilization of polysulfides. The binding energy of phosphorene dopant to various polysulfides ranged from 1 to 2.5 eV, much higher than that of bare carbons (0.5 eV). As such, the assembled Li-S battery achieved high capacity retention (>660 mAh g^{-1}) even after 500 continuous cycles' tests and exhibits a small capacity decay (0.053 % per cycle).[97, 123]

5. Flexible interfacial layers

To further tackle the electrochemical issues of Li-S batteries, it is also feasible to mount a layer of fibrous material on the surface of Li anode or S cathode as the interfacial layers. In most studies, interfacial layers are named as buffer layers and interlayers for the Li anodes and S cathodes, respectively. The interlayers can be also attached on the separators for Li-S batteries. Additionally, because SSEs can simultaneously relieve the formation of Li dendrites and

dissolution of soluble polysulfides, they are also regarded as efficient interfacial layers in Li-S batteries in this section. Materials including fibrous carbons,[124, 125] polymer fibers (*e.g.*, polyacrylonitrile nanofiber),[126-128] and ceramic fibers (*e.g.*, glass fibers, $Li_7La_3Zr_2O_{12}$ (LLZO) fibers)[23, 126, 129, 130] are mostly used in the fabrication of flexible interfacial layers. This section discusses the functionalities and advantages of interfacial layers in stabilizing the electrochemical performance of Li-S batteries.

5.1 Buffer layers of Li anodes

5.1.1 Uniform distribution of Li^+

Buffer layers can relive the formation of Li dendrites via regulating the concentration of Li^+ at the surface of Li anode. Typically, buffer layers are highly porous to provide sufficient intake of the electrolyte and ensure good ionic contact between Li anode and electrolyte. The surface of the buffer layer always possesses high densities of polar functional groups, which can interact with Li^+ to slow down the movement of Li^+ towards deposition on hot spots, such as Li dendrites or protuberances of current collectors. Liang et al. designed an oxidized polyacrylonitrile nanofiber modified with abundant polar functional groups (C=N, C-N, C=O, and O-H).[126] The good affinity between functional groups and the electrolyte benefited for the uniform distribution of Li^+, which efficiently suppressed the self-amplified growth of Li dendrites. With the assist of the buffer layer, Li anode achieved a stable CE of 97.4 % at a current density of 3 mA cm^{-2} for 120 cycles. Similarly, a 3D glass fiber (GF) with intentionally decorated polar functional groups (Si-O, O-H, and O-B) was demonstrated by Cheng et al.[131] These functional groups can adsorb considerable Li^+ to compensate the concentration gradient of Li^+ (Figure 10a). In comparison to Cu foil-based Li anode, the homogeneously distributed Li^+ enabled GF-based Li anode to achieve a largely improved CE from 80 % to 97 % @1.0 mA cm^{-2}, and provide the dendrite-free deposition even at a high rate of 10.0 mA cm^{-2} (Figure 10b).

5.1.2 Stabilization of SEI

Usually, the plating/stripping of Li causes the repeated breakage and formation of SEI. The consumption of extra Li to build new SEI largely reduces the CE (<98 %) of Li anode. To stabilize the SEI, Zhang et al. fabricated a buffer layer with a lithiophilic-lithiophobic gradient material (Figure 10c).[132] In this work, CNT film was partially deposited with zinc oxide (ZnO) to achieve a surface with a lithiophilic gradient. The bottom surface of CNT was decorated with a high concentration of ZnO, which can be tightly anchored onto underneath Li foil due to its high lithiophilicity. The seamless interfacial contact between the Li foil and buffer layer favored Li anode to form a uniform and stable SEI layer. Such a buffer layer integrated various advantages for protecting Li anode, including the stabilization of SEI and acceleration of diffusion of Li^+. Both the advantages effectively suppressed the growth of dendrites, which benefited the Li anode to achieve a remarkable CE $\approx$99.5 % at 2 mA cm^{-2} for 100 cycles (Figure 10d).

5.2 Interlayers of S cathodes

Fibrous interlayers of S cathodes can suppress the shuttle effect, accelerate the sluggish kinetics of redox reaction, and accommodate the volumetric change of different S species. Table 1 summarizes the functionalities of interlayers of S cathodes. It also compares the battery performances with or without these interlayers.

5.2.1 Suppression of shuttle effect

Similar to fibrous current collectors, the mechanisms of physisorption and chemisorption are also adaptable to fibrous interlayers for the anchor of soluble polysulfides. Fibrous interlayers modified with polar metal compounds, such as MnO_2, TiO_2, Ti_4O_7, V_2O_5, HfO_2, and WS_2 are

certified to provide strong chemisorption. The examples include MWCNTs/MnO$_2$, TiO$_2$/cellulose fiber, and V$_2$O$_5$ NW/GNS hybrid, etc.[72, 133, 134] Recently, a praline-like interlayer containing TiO$_2$ nanoparticles decorated CNF was reported by Zhao et al.[135] The embedded TiO$_2$ mitigated the dissolution of polysulfides by forming Ti-S interaction. It also confined the absorbed S species on the well-dispersed active sites to prevent the aggregation of these cathodic materials (Figure 11a). The incorporation of such an interlayer led to the significant enhancement of cycling stability, of which the S cathode showed a 25 % higher capacity retention (62 % after 300 cycles) than the cathode without interlayer (Figure 11b).

5.2.2 Accommodation of volumetric change

The S cathode exhibits a volumetric expansion (80 %) during transition among different S species. To accommodate the volumetric change, Cao et al. designed a flexible and elastic interlayer made with N-doped CNF-CNT (NCF-CNT) (Figure 11c).[94] The advantage of using such an elastic interlayer was verified by the marginal change of color of separators after cycling test. The separator with upside near the cathode of the Al-CNT/S battery exhibited a bleached color from the edge to the center. The yellow substance on the surface of the separator can be indexed to the polysulfides, which dissolved into the electrolyte and captured by the separator. In stark contrast, no visible yellowish substance occurred on the surface of the separator for the NCF-CNT/S battery. Such a result can be attributed to the excellent capability of shape recovery of the elastic interlayer, which well confined the S species inside its porous architecture during the cycling test. The NCF-CNT also provided numerous open channels for the easy access of electrolyte. All these appealing structural properties favored S cathode to achieve a high CE of 98.6 %, an excellent rate capability of 691.8 mAh g^{-1} @2 C and remain a high specific capacity of 902.8 mAh g^{-1} after 100 cycles (Figure 11d).

5.2.3 Acceleration of redox reaction

Although the soluble polysulfides can be captured by the anchoring materials (*e.g.* metal oxides, metal sulfides) on the interfacial layers, seldom can they convert into low order of polysulfides (*e.g.* from Li_2S_6 to Li_2S_4) due to the sluggish kinetics of the conversion reaction. As such, interlayers with catalytic functions are highly demanded. So far, materials including phosphorene, CoS_2, TiC, Pt nanoparticle, P_2S_5, and cysteamine-sulfhydryl functional groups have been demonstrated efficiency to promote the redox reaction of Li-S batteries.[105, 123, 136-141] Among those, flexible interlayer made with WS_2-supported carbon cloth showed desirable acceleration of the conversion of polysulfides.[142] In this work, the carbon cloth acted as an electrically conductive matrix to enhance the transport of electrons, while WS_2 particles functioned as both absorbers and catalysis of the soluble Li_2S_n (Figure 11e). The use of such an interlayer enabled a transparent electrolyte of the vial cell after cycling test, showing a stark contrast to the yellowish color of the electrolyte of the vial cell without interlayer (Figure 11f and g). Owing to the multi-functionality of the interlayer, soluble polysulfides were efficiently trapped and converted to low-order polysulfides. Consequently, the S cathode displayed excellent cycling performance (500 cycles) with a high capacity retention of 72.5 % (1000 mAh g^{-1} @0.5 C) (Figure 11h).

5.3 Solid-state electrolytes

Other than using buffer layers or interlayers, another valid solution to deal with the electrochemical/mechanical issues of Li-S batteries is the construction of flexible SSEs. SSEs can simultaneously suppress the formation of Li dendrites and relieve the dissolution of soluble polysulfides by taking the advantages of their solid characteristics and high shear modulus. Besides, SSEs are thermostable to resolve the safety issue occurred in the liquid electrolyte-based Li-S batteries.[44, 143, 144] In addition to these superiorities, fibrous SSEs can also enlarge

the contact surface area between the electrode and the electrolyte, ensuring stable electrochemical performances of solid-state Li-S batteries. Till now, fibrous SSEs for flexible Li-S batteries mainly include oxide solid electrolytes, sulfide solid electrolytes, and composite polymer electrolytes.[144-148]

5.3.1 Fabrication techniques

Fibrous oxide solid electrolytes can be synthesized via high-temperature calcination and spinning (wet/melt spinning, electrospinning).[23, 146, 147, 149] Particularly, spinning results in fiber-shaped electrolytes with suitable lengths and desirable diameters. The fiber-shaped electrolytes can be further woven into cloth-like mats via conventional textile processing.[149] Sulfide solid electrolytes are mostly prepared under inert atmosphere since they are highly reactive with humid air. Techniques for fabricating sulfide solid electrolytes include melt-quenching, ball-milling reactions, and wet chemical reactions. Among those, wet chemical reaction circumvents high-temperature treatment or prolonged mechanical mixing, which shows good cost-effectiveness.[150] Both oxide- and sulfide solid electrolytes can be mixed with Li^+ conductive polymers to yield composite polymer electrolytes.

5.3.2 Oxide solid electrolytes

The typical oxide solid electrolytes consist of perovskite-type $Li_{0.33}La_{0.557}TiO_3$ (LLTO), NASICON-like $Li_{1.3}Al_{0.3}Ti_{1.7}(PO_4)_3$ (LATP), and garnet-type $Li_7La_3Zr_2O_{12}$ (LLZO). They can accommodate a large amount of Li^+ with their unique crystalline structures, hence making them highly ionic conductive (*e.g.*, bulk LLZO: 10^{-4}-10^{-3} S cm^{-1} at room temperature).[151] However, both LATP and LLTO are electrochemically unstable due to the reduction of Ti^{4+} at 2.5 and 1.8 V vs. Li, respectively: Li^+ irreversibly intercalates into ceramic fibers, generating a phase transition of the electrolyte. As such, both LATP and LLTO are not suitable in Li-S batteries

with the operation voltage of 1.7-2.8 V.[129, 152] In stark contrast, garnet-type LLZO fibers present a larger electrochemically stable voltage window than LLTO and LATP fibers, which endows them good compatibility with Li-S batteries.[153-155] Gong et al. prepared a Li$^+$ conductive ceramic textile (2.7×10^{-5} S cm^{-1}) via one-step calcination of cellulose textiles that soaked with the LLZO precursor (Figure 12a).[146] The resultant garnet textile possessed a multi-scale porosity and a high surface/volume ratio, making it easy for the infiltration of S with a high mass loading of 10.8 g cm^{-2} (Figure 12b and c). Such a flexible oxide solid electrolyte further provided good electrochemical stability when used in the solid-state Li-S battery. For instance, the battery delivered a high capacity of 1000 mAh g^{-1} and run for 40 cycles (Figure 12d).

5.3.3 sulfide solid electrolytes

Recently, there has been an increasing interest in sulfide solid electrolytes, such as thio-LISICON (*e.g.*, Li$_{3.25}$Ge$_{0.25}$P$_{0.75}$S$_4$ (LGPS)), glass-ceramic Li$_2$S-P$_2$S$_5$ (e.g., Li$_7$P$_3$S$_{11}$, 70Li$_2$S-30P$_2$S$_5$), and anion-doped Li$_2$S-P$_2$S$_5$.[156-158] The replacement of O^{2-} in the oxide solid electrolytes by S^{2-} can effectively enhance the capability of Li$^+$ transport in the sulfide solid electrolytes, since S^{2-}owns a larger ionic radius and shows better polarization capability, which can weaken the interaction between Li$^+$ and anionic molecules. As such, sulfide solid electrolytes normally have higher ionic conductivity (10^{-3}-10^{-2} S cm^{-1} at room temperature) than that of oxide solid electrolytes.[158] Moreover, sulfide solid electrolytes present better ductility than oxide solid electrolyte, which enables the intimate contact with the active materials by means of simple cold pressing.[144, 148, 150, 159] Although fibrous sulfide solid electrolytes are still under investigation, many researchers have already demonstrated the good performance of sulfide solid electrolytes by mixing them with fibrous skeletons.[144, 148] Very recently, Xu et al. described a thin and solid Li$_3$PS$_4$ electrolyte reinforced by fibrous Kevlar nonwoven with an

ionic conductivity of 3×10^{-4} S cm^{-1} (Fig. 12e). The ion-insulating Kevlar nonwoven provided mechanical support to well protect the electrolyte from the structural break during the fabrication or operation of batteries. As a result, the solid-state Li-Li$_2$S battery presented good stability during the cycling test. The device also achieved a highly reversible discharge capacity of 949.9 mAh g^{-1} @0.05 C (Fig. 12f), and a high energy density of 370.6 Wh kg^{-1}.[144]

5.3.4 Composite polymer electrolytes

Composite polymer electrolytes that contain polymers, Li salts, inorganic fillers represents a more feasible technology to realize flexible Li-S batteries. On one hand, composite polymer electrolytes are more flexible than the inorganic solid electrolytes due to the low Young's modulus of the polymer hosts. On the other hand, composite polymer electrolytes have higher ionic conductivity and better structural stability than bare polymer electrolytes (*e.g.*, the crystallization of poly (ethylene oxide) (PEO) electrolyte restricts the segmental movements for transportion of Li$^+$ at ambient temperature).[143] All these advantages ensure the reliability of composite polymer electrolytes in the application of solid-state Li-S batteries. For demonstration, a flexible composite polymer electrolyte consisting of 3D LLZO network and polyethylene oxide (PEO) was recently fabricated.[147] The electrospun LLZO nanofibers acted as continuous channels for the transport of Li$^+$ (Figure 12g). Fibrous LLZO-based composite polymer electrolyte featured many desirable properties, such as high ionic conductivity (2.5×10^{-4} S cm^{-1}), superior compatibility with Li metal, good chemical stability against air and moisture, and remarkable structural stability. These appealing physical and chemical characteristics of composite polymer electrolyte enabled Li symmetric batteries to stably run for 500 h @0.2 mA cm^{-2} and over 300 h @5 mA cm^{-2} (Figure 12h). In a flammability test, the LLZO nanowire-reinforced composite polymer electrolyte well retained its structural integrity, while the conventional polymer/filler electrolyte was easily burnt (Figure 12i). The outstanding thermal

stability demonstrated the feasibility of such a fiber-reinforced composite polymer electrolyte for fabricating safe Li-S batteries.

6. Flexible Li-S batteries

A rational design of battery configuration also plays an important role in determining the electrochemical and mechanical performances of full batteries. In this section, several assembly methods of flexible Li-S batteries are carefully discussed.

6.1 Wire-type Li-S battery

Wire-type Li-S battery consists of a pair of fibrous Li anode and S cathode with paralleled, twisted, or coaxial alignment. These electrodes are electrically isolated by separators or SSEs and sealed in a cylindrical polymer tube.[160-162] Wire-type batteries are omnidirectionally flexible, which can survive from complicated deformations (*e.g.*, bending, twisting, folding, and tying) (Figure 13a).[88, 161, 163-167] Besides, wire-type batteries are capable of woven, knitted, or embroidered into functional textiles due to their small feature size (Figure 13b).[88]

Fang et al. reported the first example of wire-type Li-S battery by wrapping S encapsulated particles inside lightweight CNT fibers (68 wt% for S).[88] To standardize the electrochemical performance of fibrous S cathode, a coin-type device was assembled using Li foil as the counter electrode. The device delivered an initial discharge capacity of 1051 mAh g^{-1} @0.1 C (normalized to S), and high capacity retention of 83.9 % after 100 cycles. To test the electrochemical performance of a wire-type device, Chong et al. reported a wet spinning method to prepare highly conductive rGO/CNT/S hybrid cathode (45 wt% for S).[168] Such a cathode was then paired with Li wire to fabricate a wire-type Li-S battery. The full cell obtained an initial discharge capacity of 762 mAh g^{-1} @0.1 C and can power the LED with a marginal drop in power intensities upon flexing (Figure 13c). However, the device exhibited a fast

capacity decay after only 3 cycles, likely due to the impeded diffusion of Li^+ by the uncontrollable stacking of rGO layers in the S cathode.

To achieve a wire-type Li-S battery with a long lifespan and high capacity retention, a freestanding nanostructured rGO/S composite cathode was reported by Cao et al.[169] rGO/S presented an interconnected architecture, making it strong enough to prevent the stacking of rGO layers. Besides, this composite cathode was highly porous to facilitate the diffusion of Li^+. Both advantages enabled a high initial discharge capacity over 1300 mAh g^{-1} and high capacity retention after 50 cycles' test (Figure 13d).

6.2 Li-S battery with integrated architecture

The seamless integration of different battery components into a monolithic architecture enhances the mechanical stability of the battery. Such an architecture also contributes to a higher specific energy density of the battery by reducing its inactive volume/weight. To prove such a concept, Wang et al. designed an integrated cathode consisting of a carbon/S/carbon spread directly on the separator (CSC @separator) (Figure 14a).[170] Due to the absence of Al foil, the CSC @separator achieved a largely reduced weight by 78 % and exhibited excellent flexibility. The double-layered fibrous carbon accelerated the transport of electrons, physically shut the diffusion of polysulfides, and buffered the volumetric expansion of the cathodic materials. This cathode achieved a largely enhanced reversible capacity of 730 mAh g^{-1} over 500 cycles, together with a smaller capacity decay (0.058 % per cycle) in comparison with the cathodes of S @Al, S @separator, SC @separator, CS @separator (Figure 14b).

The design of integrated architecture can also reduce the interfacial resistance among different battery components. In a recent work, Zhu et al. reported a bilayer framework by integrating the S cathode with composite polymer electrolyte via direct casting of PEO/LLTO solution onto the CNF/S cathode.[171] This bilayer structure presented an intimate contact among

the conductive matrix (CNF), active material (S) and electrolyte (LLTO/PEO) (Figure 14c), which ensured fast transport of both electrons and Li^+. The solid-state Li-S battery assembled with such a bilayer (mass loading of S is 1.27 mg cm^{-2}) showed a stable cycling performance with a capacity retention of 415 mAh g^{-1} @0.05 C, and a CE over 99 % after 50 cycles (Figure 14d). Inspired by these works, other integrated architectures such as bilayer framework (cathode/separator),[42] three-in-one (cathode/interlayer/separator) membrane,[172] and all-in-one (cathode/separator/anode)[72] configuration were also developed.

6.3 Foldable Li-S battery

The next generation of deformable electronics will need to be powered by batteries that are not only flexible but also foldable.[53, 80, 173] However, two formidable challenges hinder the development of foldable Li-S batteries, including 1) the plastic deformation of current collectors when folded. 2) the crack of active materials, or the delamination of active materials from the surface of respective current collectors. A promising solution to address the above challenges would be redesigning the battery architecture so as to avoid large strains on the active materials when the battery is bent. As a proof of concept, Li et al. impregnated S and Li into the super-elastic CNTs network and fabricated them into a checkboard pattern (Figure 15a).[173] The molecular dynamics (MD) simulation indicated that the CNTs network was able to withstand higher stresses associated with folding without significant plastic deformation in comparison with an individual CNT (Figure 15b and c). In addition, the unique pattern enabled the battery to be folded along mutually orthogonal directions. During the folding test, the strain was mainly absorbed by the highly flexible and elastic CNTs rather than Li or S. Therefore, the foldable Li-S battery delivered a stable areal capacity of 3 mAh cm^{-2} and achieved a capacity loss of <12 % over 100 continuous folding and unfolding cycles.

The use of intrinsically soft and highly conductive fabrics represents another viable solution for fabricating foldable batteries. Fabric-type batteries can effectively accommodate the complex deformations induced by body motion and are easy to integrate into the ordinary cloth. For the first time, Chang et al. developed a fabric-type Li-S battery comprising both fabric Li anode and S cathode (Figure 15d).[74] In such a device, the CuCF and NiCF worked as the current collectors of Li anode and S cathode, respectively. These metallic fabrics were highly conductive and exhibited excellent flexibility (Figure 15e and f). For instance, the CuCF showed a low sheet resistance of 0.1 Ω sq^{-1} and little conductivity change after flexing for 5000 cycles at a very small bending radius of 2.5 mm. As such, the as-fabricated fabric-type Li-S battery exhibited a marginal areal capacity decay after 100 cycles of flexing at a small radius of 5 mm (Figure 15g) and can even withstand 40 repeated folds at a bending radius of <1 mm (Figure 15h).

7. Conclusions and Outlook

We have reviewed the recent progress of fibrous materials for flexible Li-S batteries. Owing to the desirable structural properties and diverse functionalities of fibrous materials, remarkable progress has been made in fibrous Li anodes and S cathodes with respect to their outstanding electrochemical and mechanical performances (large areal capacity, high CE, low capacity decay, and good flexibility). Considering further enhancements of the battery performance and practical applications of flexible Li-S batteries, more explorations are expected in following directions with the collaboration of academia and industry.

SSEs are more suitable than liquid electrolytes for fabricating safe and flexible Li-S batteries. However, reported fibrous SSEs nowadays typically display much lower ionic conductivity (in the range of <10^{-3} S cm^{-1}) than that of the organic liquid system (~10^{-2} S cm^{-1}). In addition, SSEs tends to introduce large interfacial resistance between SSEs and Li or S electrode, which

poses a large voltage hysteresis and poor rate performance of solid-state Li-S batteries. Therefore, desirable fibrous SSEs should be highly ionically conductive (competitive with the liquid system) and can seamlessly integrate with flexible Li and S electrodes.

The energy density and flexibility of Li-S batteries are determined by the package materials. So far, commercial Al plastic is the major package material because of its good airtightness and low cost. However, Al plastic is typically thick and rigid, which can not withstand rigorous mechanical deformation. Although polyolefin tube has been reported as flexible package material for wire-type Li-S batteries, the high air and moisture permeability hinders its practical applications in the flexible Li-S batteries. Therefore, encapsulation hosts with good airtightness, lightweight, small volume, and good flexibility are strongly requested.

According to the industrial requirements, flexible batteries should simultaneously achieve a volumetric energy density > 350 Wh L^{-1} and survive from a minimum bending cycle of 1000 for powering the smartwatch. These values increase to > 400 Wh L^{-1} (1000 cycle), >500 Wh L^{-1} (2000 cycle), and > 660 Wh L^{-1} (2000 cycle) for the wearable heaters, bendable phones, and rolled-up displays, respectively.[41, 174, 175] There is hardly any Li-S coin cell that can achieve the above-mentioned performance, not to mention flexibility. Therefore, it is very challenging to achieve long-term cycling stability of Li-S batteries. Fibrous materials indeed, as we discussed in the previous sections, can provide vital contribution to stabilizing both Li anode and S cathode, and at the same time, offer suitable flexibility. The design of the better cells requires further exploration and optimization from conventional thin film stacks to composite-like structures. There are also critical technical challenges on how to adapt lab-scale performances of flexible Li-S batteries (tested based on coin cells or small pouch cells) to scaled-up and commercialized production lines in the future.

References

[1]   R. F. Service, *Science* **2003**, *301*, 909.

[2]   B. C.-K. Tee, A. Chortos, A. Berndt, A. K. Nguyen, A. Tom, A. McGuire, Z. C. Lin, K. Tien, W.-G. Bae, H. Wang, *Science* **2015**, *350*, 313-316.

[3]   D.-H. Kim, N. Lu, R. Ma, Y.-S. Kim, R.-H. Kim, S. Wang, J. Wu, S. M. Won, H. Tao, A. Islam, *Science* **2011**, *333*, 838-843.

[4]   W. Gao, S. Emaminejad, H. Y. Y. Nyein, S. Challa, K. Chen, A. Peck, H. M. Fahad, H. Ota, H. Shiraki, D. Kiriya, *Nature* **2016**, *529*, 509-514.

[5]   S. Bae, H. Kim, Y. Lee, X. Xu, J.-S. Park, Y. Zheng, J. Balakrishnan, T. Lei, H. R. Kim, Y. I. Song, *Nat. Nanotechnol.* **2010**, *5*, 574.

[6]   A. M. Gaikwad, B. V. Khau, G. Davies, B. Hertzberg, D. A. Steingart, A. C. Arias, *Adv. Energy Mater.* **2015**, *5*, 1401389.

[7]   A. M. Gaikwad, G. L. Whiting, D. A. Steingart, A. C. Arias, *Adv. Mater.* **2011**, *23*, 3251-3255.

[8]   S. W. Kim, J. H. Yun, B. Son, Y. G. Lee, K. M. Kim, Y. M. Lee, K. Y. Cho, *Adv. Mater.* **2014**, *26*, 2977-2982.

[9]   M. Koo, K.-I. Park, S. H. Lee, M. Suh, D. Y. Jeon, J. W. Choi, K. Kang, K. J. Lee, *Nano Lett.* **2012**, *12*, 4810-4816.

[10]   X. Liao, C. Shi, T. Wang, B. Qie, Y. Chen, P. Yang, Q. Cheng, H. Zhai, M. Chen, X. Wang, *Adv. Energy Mater.* **2019**, *9*, 1802998.

[11]   H.-J. Peng, J.-Q. Huang, Q. Zhang, *Chem. Soc. Rev.* **2017**, *46*, 5237-5288.

[12]   H. J. Peng, J. Q. Huang, X. B. Cheng, Q. Zhang, *Adv. Energy Mater.* **2017**, *7*, 1700260.

[13]   A. Manthiram, Y. Fu, S.-H. Chung, C. Zu, Y.-S. Su, *Chem. Rev.* **2014**, *114*, 11751-11787.

[14]   J. Liu, Z. Bao, Y. Cui, E. J. Dufek, J. B. Goodenough, P. Khalifah, Q. Li, B. Y. Liaw, P. Liu, A. Manthiram, *Nat. Energy* **2019**, *4*, 180-186.

[15]   D. Lin, Y. Liu, Y. Cui, *Nat. Nanotechnol.* **2017**, *12*, 194.

[16]   S. Xia, X. Wu, Z. Zhang, Y. Cui, W. Liu, *Chem* **2019**, *5*, 753-785.

[17]   M. A. Pope, I. A. Aksay, *Adv. Energy Mater.* **2015**, *5*, 1500124.

[18]   Z. W. Seh, Y. Sun, Q. Zhang, Y. Cui, *Chem. Soc. Rev.* **2016**, *45*, 5605-5634.

[19]   Y. Yang, G. Zheng, Y. Cui, *Chem. Soc. Rev.* **2013**, *42*, 3018-3032.

[20]   Q. Huang, D. Wang, Z. Zheng, *Adv. Energy Mater.* **2016**, *6*, 1600783.

[21]   L. Liu, Y. Yu, C. Yan, K. Li, Z. Zheng, *Nat. Commun.* **2015**, *6*, 1-9.

[22]   K. Jiang, J. Wang, Q. Li, L. Liu, C. Liu, S. Fan, *Adv. Mater.* **2011**, *23*, 1154-1161.

[23]   W. Liu, S. W. Lee, D. Lin, F. Shi, S. Wang, A. D. Sendek, Y. Cui, *Nat. Energy* **2017**, *2*, 1-7.

[24]   Q. Li, S. Zhu, Y. Lu, *Adv. Funct. Mater.* **2017**, *27*, 1606422.

[25]   H. Lee, M. Yanilmaz, O. Toprakci, K. Fu, X. Zhang, *Energy Environ. Sci.* **2014**, *7*, 3857-3886.

[26]   P.-L. Taberna, S. Mitra, P. Poizot, P. Simon, J.-M. Tarascon, *Nat. Mater.* **2006**, *5*, 567-573.

[27]   A. Vlad, A. L. M. Reddy, A. Ajayan, N. Singh, J.-F. Gohy, S. Melinte, P. M. Ajayan, *Proc. Natl. Acad. Sci.* **2012**, *109*, 15168-15173.

[28]   C. Hwang, W. J. Song, J. G. Han, S. Bae, G. Song, N. S. Choi, S. Park, H. K. Song, *Adv. Mater.* **2018**, *30*, 1705445.

[29]   C. Xu, J. Liao, C. Yang, R. Wang, D. Wu, P. Zou, Z. Lin, B. Li, F. Kang, C.-P. Wong, *Nano Energy* **2016**, *30*, 900-908.

[30]   W. Wang, M. Tian, A. Abdulagatov, S. M. George, Y.-C. Lee, R. Yang, *Nano Lett.* **2012**, *12*, 655-660.

[31]   K. Liu, B. Kong, W. Liu, Y. Sun, M.-S. Song, J. Chen, Y. Liu, D. Lin, A. Pei, Y. Cui, *Joule* **2018**, *2*, 1857-1865.

[32]   H. Li, Z. Tang, Z. Liu, C. Zhi, *Joule* **2019**, *3*, 613-619.

[33]   X. Wang, Z. Pan, J. Yang, Z. Lyu, Y. Zhong, G. Zhou, Y. Qiu, Y. Zhang, J. Wang, W. Li, *Energy Storage Mater.* **2019**, *22*, 179-184.

[34]   X. Tao, *Acc. Chem. Res.* **2019**, *52*, 307-315.

[35]   W. Yan, C. Dong, Y. Xiang, S. Jiang, A. Leber, G. Loke, W. Xu, C. Hou, S. Zhou, M. Chen, *Mater. Today* **2020**.

[36]   W. Zeng, L. Shu, Q. Li, S. Chen, F. Wang, X. M. Tao, *Adv. Mater.* **2014**, *26*, 5310-5336.

[37]   G. Li, S. Wang, Y. Zhang, M. Li, Z. Chen, J. Lu, *Adv. Mater.* **2018**, *30*, 1705590.

[38]   D. Su, D. Zhou, C. Wang, G. Wang, *Adv. Funct. Mater.* **2018**, *28*, 1800154.

[39]   A. M. Gaikwad, A. C. Arias, D. A. Steingart, *Energy Technol.* **2015**, *3*, 305-328.

[40]   A. M. Gaikwad, A. C. Arias, *ACS Appl. Mater. Interfaces* **2017**, *9*, 6390-6400.

[41]   J. Chang, Q. Huang, Z. Zheng, *Joule* **2020**.

[42]   J.-H. Kim, Y.-H. Lee, S.-J. Cho, J.-G. Gwon, H.-J. Cho, M. Jang, S.-Y. Lee, S.-Y. Lee, *Energy Environ. Sci.* **2019**, *12*, 177-186.

[43]   A. Wang, S. Tang, D. Kong, S. Liu, K. Chiou, L. Zhi, J. Huang, Y. Y. Xia, J. Luo, *Adv. Mater.* **2018**, *30*, 1703891.

[44]   Q. Zhao, S. Stalin, C.-Z. Zhao, L. A. Archer, *Nat. Rev. Mater.* **2020**, 1-24.

[45]   J. W. Long, B. Dunn, D. R. Rolison, H. S. White, *Chem. Rev.* **2004**, *104*, 4463-4492.

[46]   L. M. Ericson, H. Fan, H. Peng, V. A. Davis, W. Zhou, J. Sulpizio, Y. Wang, R. Booker, J. Vavro, C. Guthy, *Science* **2004**, *305*, 1447-1450.

[47]   D. Yu, K. Goh, H. Wang, L. Wei, W. Jiang, Q. Zhang, L. Dai, Y. Chen, *Nat. Nanotechnol.* **2014**, *9*, 555.

[48]   V. A. Davis, A. N. G. Parra-Vasquez, M. J. Green, P. K. Rai, N. Behabtu, V. Prieto, R. D. Booker, J. Schmidt, E. Kesselman, W. Zhou, *Nat. Nanotechnol.* **2009**, *4*, 830-834.

[49]   S. M. Cooper, H. F. Chuang, M. Cinke, B. A. Cruden, M. Meyyappan, *Nano Lett.* **2003**, *3*, 189-192.

[50]   L. F. Chen, Y. Feng, H. W. Liang, Z. Y. Wu, S. H. Yu, *Adv. Energy Mater.* **2017**, *7*, 1700826.

[51]   Q. Dong, G. Wang, H. Hu, J. Yang, B. Qian, Z. Ling, J. Qiu, *J. Power Sources* **2013**, *243*, 350-353.

[52]   F. Jin, S. Xiao, L. Lu, Y. Wang, *Nano Lett.* **2016**, *16*, 440-447.

[53]   C.-H. Chang, S.-H. Chung, A. Manthiram, *Mater. Horiz.* **2017**, *4*, 249-258.

[54]   L. Sun, M. Li, Y. Jiang, W. Kong, K. Jiang, J. Wang, S. Fan, *Nano Lett.* **2014**, *14*, 4044-4049.

[55]   G. Zhou, D.-W. Wang, F. Li, P.-X. Hou, L. Yin, C. Liu, G. Q. M. Lu, I. R. Gentle, H.-M. Cheng, *Energy Environ. Sci.* **2012**, *5*, 8901-8906.

[56]   L. Q. Zhang, X. H. Liu, Y. Liu, S. Huang, T. Zhu, L. Gui, S. X. Mao, Z. Z. Ye, C. M. Wang, J. P. Sullivan, *ACS Nano* **2011**, *5*, 4800-4809.

[57]   R. Liu, Y. Liu, J. Chen, Q. Kang, L. Wang, W. Zhou, Z. Huang, X. Lin, Y. Li, P. Li, *Nano Energy* **2017**, *33*, 325-333.

[58]   Y.-H. Lee, J.-S. Kim, J. Noh, I. Lee, H. J. Kim, S. Choi, J. Seo, S. Jeon, T.-S. Kim, J.-Y. Lee, *Nano Lett.* **2013**, *13*, 5753-5761.

[59]   D. Wang, Y. Zhang, X. Lu, Z. Ma, C. Xie, Z. Zheng, *Chem. Soc. Rev.* **2018**, *47*, 4611-4641.

[60]   P. Li, Y. Zhang, Z. Zheng, *Adv. Mater.* **2019**, *31*, 1902987.

[61]   X. Zhang, A. Wang, X. Liu, J. Luo, *Acc. Chem. Res.* **2019**, *52*, 3223-3232.

[62]   P. Bai, J. Li, F. R. Brushett, M. Z. Bazant, *Energy Environ. Sci.* **2016**, *9*, 3221-3229.

[63]   L. Liu, Y.-X. Yin, J.-Y. Li, N.-W. Li, X.-X. Zeng, H. Ye, Y.-G. Guo, L.-J. Wan, *Joule* **2017**, *1*, 563-575.

[64]   T. T. Zuo, X. W. Wu, C. P. Yang, Y. X. Yin, H. Ye, N. W. Li, Y. G. Guo, *Adv. Mater.* **2017**, *29*, 1700389.

[65]   F. Shen, F. Zhang, Y. Zheng, Z. Fan, Z. Li, Z. Sun, Y. Xuan, B. Zhao, Z. Lin, X. Gui, *Energy Storage Mater.* **2018**, *13*, 323-328.

[66]   G. Yang, Y. Li, Y. Tong, J. Qiu, S. Liu, S. Zhang, Z. Guan, B. Xu, Z. Wang, L. Chen, *Nano Lett.* **2018**, *19*, 494-499.

[67]   S. Jin, S. Xin, L. Wang, Z. Du, L. Cao, J. Chen, X. Kong, M. Gong, J. Lu, Y. Zhu, *Adv. Mater.* **2016**, *28*, 9094-9102.

[68]   L. Hu, J. W. Choi, Y. Yang, S. Jeong, F. La Mantia, L.-F. Cui, Y. Cui, *Proc. Natl. Acad. Sci.* **2009**, *106*, 21490-21494.

[69]   L.-L. Lu, J. Ge, J.-N. Yang, S.-M. Chen, H.-B. Yao, F. Zhou, S.-H. Yu, *Nano Lett.* **2016**, *16*, 4431-4437.

[70]   C.-P. Yang, Y.-X. Yin, S.-F. Zhang, N.-W. Li, Y.-G. Guo, *Nat. Commun.* **2015**, *6*, 1-9.

[71]   K. Yan, B. Sun, P. Munroe, G. Wang, *Energy Storage Mater.* **2018**, *11*, 127-133.

[72]   M. Yao, R. Wang, Z. Zhao, Y. Liu, Z. Niu, J. Chen, *ACS Nano* **2018**, *12*, 12503-12511.

[73]   Y. Liu, D. Lin, Z. Liang, J. Zhao, K. Yan, Y. Cui, *Nat. Commun.* **2016**, *7*, 10992.

[74]   J. Chang, J. Shang, Y. Sun, L. K. Ono, D. Wang, Z. Ma, Q. Huang, D. Chen, G. Liu, Y. Cui, *Nat. Commun.* **2018**, *9*, 1-11.

[75]   C. Niu, H. Pan, W. Xu, J. Xiao, J.-G. Zhang, L. Luo, C. Wang, D. Mei, J. Meng, X. Wang, *Nat. Nanotechnol.* **2019**, *14*, 594-601.

[76]   R. Zhang, X. Chen, X. Shen, X.-Q. Zhang, X.-R. Chen, X.-B. Cheng, C. Yan, C.-Z. Zhao, Q. Zhang, *Joule* **2018**, *2*, 764-777.

[77]   B. Yu, T. Tao, S. Mateti, S. Lu, Y. Chen, *Adv. Funct. Mater.* **2018**, *28*, 1803023.

[78]   Z. Liang, D. Lin, J. Zhao, Z. Lu, Y. Liu, C. Liu, Y. Lu, H. Wang, K. Yan, X. Tao, *Proc. Natl. Acad. Sci.* **2016**, *113*, 2862-2867.

[79]   D. Lin, Y. Liu, Z. Liang, H.-W. Lee, J. Sun, H. Wang, K. Yan, J. Xie, Y. Cui, *Nat. Nanotechnol.* **2016**, *11*, 626-632.

[80]   Y. Mao, G. Li, Y. Guo, Z. Li, C. Liang, X. Peng, Z. Lin, *Nat. Commun.* **2017**, *8*, 1-8.

[81]   G. Yang, J. Tan, H. Jin, Y. H. Kim, X. Yang, D. H. Son, S. Ahn, H. Zhou, C. Yu, *Adv. Funct. Mater.* **2018**, *28*, 1800595.

[82]   H. Pan, Z. Cheng, J. Chen, R. Wang, X. Li, *Energy Storage Mater.* **2020**, *27*, 435-442.

[83]   S. Chen, L. Qiu, H.-M. Cheng, *Chem. Rev.* **2020**, *120*, 2811-2878.

[84]   W. G. Chong, F. Xiao, S. Yao, J. Cui, Z. Sadighi, J. Wu, M. Ihsan-Ul-Haq, M. Shao, J.-K. Kim, *Nanoscale* **2019**, *11*, 6334-6342.

[85]   H. Li, H. Chen, Y. Xue, Y. Zhang, M. Zhang, W. Yu, G. Bai, K. Zhuo, Y. Zheng, *Adv. Energy Mater.* **2020**, 2001683.

[86]   Z. Yuan, H. J. Peng, J. Q. Huang, X. Y. Liu, D. W. Wang, X. B. Cheng, Q. Zhang, *Adv. Funct. Mater.* **2014**, *24*, 6105-6112.

[87]   Q. Sun, X. Fang, W. Weng, J. Deng, P. Chen, J. Ren, G. Guan, M. Wang, H. Peng, *Angew. Chem. Int. Edit.* **2015**, *54*, 10539-10544.

[88]   X. Fang, W. Weng, J. Ren, H. Peng, *Adv. Mater.* **2016**, *28*, 491-496.

[89]   Y. Chen, S. Lu, X. Wu, J. Liu, *J. Phys. Chem. C* **2015**, *119*, 10288-10294.

[90]   L. Sun, W. Kong, Y. Jiang, H. Wu, K. Jiang, J. Wang, S. Fan, *J. Mater. Chem. A* **2015**, *3*, 5305-5312.

[91]   L. Sun, D. Wang, Y. Luo, K. Wang, W. Kong, Y. Wu, L. Zhang, K. Jiang, Q. Li, Y. Zhang, *ACS Nano* **2016**, *10*, 1300-1308.

[92]   J.-Q. Huang, H.-J. Peng, X.-Y. Liu, J.-Q. Nie, X.-B. Cheng, Q. Zhang, F. Wei, *J. Mater. Chem. A* **2014**, *2*, 10869-10875.

[93]   X. Song, S. Wang, Y. Bao, G. Liu, W. Sun, L.-X. Ding, H. Liu, H. Wang, *J. Mater. Chem. A* **2017**, *5*, 6832-6839.

[94]   Z. Cao, J. Zhang, Y. Ding, Y. Li, M. Shi, H. Yue, Y. Qiao, Y. Yin, S. Yang, *J. Mater. Chem. A* **2016**, *4*, 8636-8644.

[95]   X. Zhao, M. Kim, Y. Liu, H.-J. Ahn, K.-W. Kim, K.-K. Cho, J.-H. Ahn, *Carbon* **2018**, *128*, 138-146.

[96]   Q. Pang, X. Liang, C. Kwok, L. F. Nazar, *J. Electrochem. Soc.* **2015**, *162*, A2567-A2576.

[97]   T. Z. Hou, W. T. Xu, X. Chen, H. J. Peng, J. Q. Huang, Q. Zhang, *Angew. Chem. Int. Edit.* **2017**, *56*, 8178-8182.

[98]   Y. Wang, R. Zhang, J. Chen, H. Wu, S. Lu, K. Wang, H. Li, C. J. Harris, K. Xi, R. V. Kumar, *Adv. Energy Mater.* **2019**, *9*, 1900953.

[99]   Z. Li, J. Zhang, X. W. Lou, *Angew. Chem. Int. Ed.* **2015**, *127*, 13078-13082.

[100]   J. He, L. Luo, Y. Chen, A. Manthiram, *Adv. Mater.* **2017**, *29*, 1702707.

[101] L. Kong, X. Chen, B. Q. Li, H. J. Peng, J. Q. Huang, J. Xie, Q. Zhang, *Adv. Mater.* **2018**, *30*, 1705219.

[102] Y. Yi, Z. Liu, P. Yang, T. Wang, X. Zhao, H. Huang, Y. Cheng, J. Zhang, M. Li, *Journal of Energy Chemistry* **2020**, *45*, 18-24.

[103] Y. Zhang, Z. Mu, C. Yang, Z. Xu, S. Zhang, X. Zhang, Y. Li, J. Lai, Z. Sun, Y. Yang, *Adv. Funct. Mater.* **2018**, *28*, 1707578.

[104] L. Ma, W. Zhang, L. Wang, Y. Hu, G. Zhu, Y. Wang, R. Chen, T. Chen, Z. Tie, J. Liu, *ACS Nano* **2018**, *12*, 4868-4876.

[105] Z. Yuan, H.-J. Peng, T.-Z. Hou, J.-Q. Huang, C.-M. Chen, D.-W. Wang, X.-B. Cheng, F. Wei, Q. Zhang, *Nano Lett.* **2016**, *16*, 519-527.

[106] S. Zhao, X. Tian, Y. Zhou, B. Ma, A. Natarajan, *Journal of Energy Chemistry* **2020**, *46*, 22-29.

[107] J. He, Y. Chen, A. Manthiram, *Energy Environ. Sci.* **2018**, *11*, 2560-2568.

[108] H. Yuan, H. J. Peng, B. Q. Li, J. Xie, L. Kong, M. Zhao, X. Chen, J. Q. Huang, Q. Zhang, *Adv. Energy Mater.* **2019**, *9*, 1802768.

[109] L. Chen, W. Yang, J. Liu, Y. Zhou, *Nano Res.* **2019**, *12*, 2743-2748.

[110] Y. Zhong, D. Chao, S. Deng, J. Zhan, R. Fang, Y. Xia, Y. Wang, X. Wang, X. Xia, J. Tu, *Adv. Funct. Mater.* **2018**, *28*, 1706391.

[111] H. Xu, L. Qie, A. Manthiram, *Nano Energy* **2016**, *26*, 224-232.

[112] K. Lu, H. Zhang, S. Gao, H. Ma, J. Chen, Y. Cheng, *Adv. Funct. Mater.* **2019**, *29*, 1807309.

[113] X. Song, T. Gao, S. Wang, Y. Bao, G. Chen, L.-X. Ding, H. Wang, *J. Power Sources* **2017**, *356*, 172-180.

[114] Z. Zhang, Q. Li, K. Zhang, W. Chen, Y. Lai, J. Li, *J. Power Sources* **2015**, *290*, 159-167.

[115] M. Chen, W. Xu, S. Jamil, S. Jiang, C. Huang, X. Wang, Y. Wang, H. Shu, K. Xiang, P. Zeng, *Small* **2018**, *14*, 1803134.

[116] X. Li, K. Ding, B. Gao, Q. Li, Y. Li, J. Fu, X. Zhang, P. K. Chu, K. Huo, *Nano Energy* **2017**, *40*, 655-662.

[117] B.-W. Zhang, T. Sheng, Y.-D. Liu, Y.-X. Wang, L. Zhang, W.-H. Lai, L. Wang, J. Yang, Q.-F. Gu, S.-L. Chou, *Nat. Commun.* **2018**, *9*, 1-11.

[118] L. Zeng, Y. Jiang, J. Xu, M. Wang, W. Li, Y. Yu, *Nanoscale* **2015**, *7*, 10940-10949.

[119] F. Wu, L. Shi, D. Mu, H. Xu, B. Wu, *Carbon* **2015**, *86*, 146-155.

[120] Y. He, M. Li, Y. Zhang, Z. Shan, Y. Zhao, J. Li, G. Liu, C. Liang, Z. Bakenov, Q. Li, *Adv. Funct. Mater.* **2020**, *30*, 2000613.

[121] F. He, J. Ye, Y. Cao, L. Xiao, H. Yang, X. Ai, *ACS Appl. Mater. Interfaces* **2017**, *9*, 11626-11633.

[122] Y. Liu, G. Li, Z. Chen, X. Peng, *J. Mater. Chem. A* **2017**, *5*, 9775-9784.

[123] L. Li, L. Chen, S. Mukherjee, J. Gao, H. Sun, Z. Liu, X. Ma, T. Gupta, C. V. Singh, W. Ren, *Adv. Mater.* **2017**, *29*, 1602734.

[124] L. Chai, J. Wang, H. Wang, L. Zhang, W. Yu, L. Mai, *Nano Energy* **2015**, *17*, 224-232.

[125] D. Zhang, Y. Zhou, C. Liu, S. Fan, *Nanoscale* **2016**, *8*, 11161-11167.

[126] Z. Liang, G. Zheng, C. Liu, N. Liu, W. Li, K. Yan, H. Yao, P.-C. Hsu, S. Chu, Y. Cui, *Nano Lett.* **2015**, *15*, 2910-2916.

[127] C. Li, B. Qin, Y. Zhang, A. Varzi, S. Passerini, J. Wang, J. Dong, D. Zeng, Z. Liu, H. Cheng, *Adv. Energy Mater.* **2019**, *9*, 1803422.

[128] Y. He, J. Wang, Y. Zhang, S. Huo, D. Zeng, Y. Lu, Z. Liu, D. Wang, H. Cheng, *J. Mater. Chem. A* **2020**.

[129] A. La Monaca, A. Paolella, A. Guerfi, F. Rosei, K. Zaghib, *Electrochem. Commun.* **2019**, 106483.

[130]   G. Lancel, P. Stevens, G. l. Toussaint, M. Maréchal, N. Krins, D. Bregiroux, C. Laberty-Robert, *Langmuir* **2017**, *33*, 9288-9297.

[131]   X. B. Cheng, T. Z. Hou, R. Zhang, H. J. Peng, C. Z. Zhao, J. Q. Huang, Q. Zhang, *Adv. Mater.* **2016**, *28*, 2888-2895.

[132]   H. Zhang, X. Liao, Y. Guan, Y. Xiang, M. Li, W. Zhang, X. Zhu, H. Ming, L. Lu, J. Qiu, *Nat. Commun.* **2018**, *9*, 1-11.

[133]   C.-Y. Fan, S.-Y. Liu, H.-H. Li, H.-F. Wang, H.-C. Wang, X.-L. Wu, H.-Z. Sun, J.-P. Zhang, *ACS Appl. Mater. Interfaces* **2016**, *8*, 28689-28699.

[134]   Y. Guo, Y. Zhang, Y. Zhang, M. Xiang, H. Wu, H. Liu, S. Dou, *J. Mater. Chem. A* **2018**, *6*, 19358-19370.

[135]   T. Zhao, Y. Ye, C. Y. Lao, G. Divitini, P. R. Coxon, X. Peng, X. He, H. K. Kim, K. Xi, C. Ducati, *Small* **2017**, *13*, 1700357.

[136]   X. Liang, C. Hart, Q. Pang, A. Garsuch, T. Weiss, L. F. Nazar, *Nat. Commun.* **2015**, *6*, 1-8.

[137]   C. Zheng, S. Niu, W. Lv, G. Zhou, J. Li, S. Fan, Y. Deng, Z. Pan, B. Li, F. Kang, *Nano Energy* **2017**, *33*, 306-312.

[138]   H. J. Peng, G. Zhang, X. Chen, Z. W. Zhang, W. T. Xu, J. Q. Huang, Q. Zhang, *Angew. Chem. Int. Edit.* **2016**, *55*, 12990-12995.

[139]   H. Al Salem, G. Babu, C. V. Rao, L. M. R. Arava, *J. Am. Chem. Soc.* **2015**, *137*, 11542-11545.

[140]   Z. Lin, Z. Liu, W. Fu, N. J. Dudney, C. Liang, *Angew. Chem. Int. Edit.* **2013**, *52*, 7460-7463.

[141]   N. Xu, T. Qian, X. Liu, J. Liu, Y. Chen, C. Yan, *Nano Lett.* **2017**, *17*, 538-543.

[142]   J. Park, B. C. Yu, J. S. Park, J. W. Choi, C. Kim, Y. E. Sung, J. B. Goodenough, *Adv. Energy Mater.* **2017**, *7*, 1602567.

[143]   S. Li, S. Q. Zhang, L. Shen, Q. Liu, J. B. Ma, W. Lv, Y. B. He, Q. H. Yang, *Adv. Sci.* **2020**, 1903088.

[144]   R. Xu, J. Yue, S. Liu, J. Tu, F. Han, P. Liu, C. Wang, *ACS Energy Lett.* **2019**, *4*, 1073-1079.

[145]   D. Li, L. Chen, T. Wang, L.-Z. Fan, *ACS Appl. Mater. Interfaces* **2018**, *10*, 7069-7078.

[146]   Y. Gong, K. Fu, S. Xu, J. Dai, T. R. Hamann, L. Zhang, G. T. Hitz, Z. Fu, Z. Ma, D. W. McOwen, *Mater. Today* **2018**, *21*, 594-601.

[147]   K. K. Fu, Y. Gong, J. Dai, A. Gong, X. Han, Y. Yao, C. Wang, Y. Wang, Y. Chen, C. Yan, *Proc. Natl. Acad. Sci.* **2016**, *113*, 7094-7099.

[148]   Y. J. Nam, S.-J. Cho, D. Y. Oh, J.-M. Lim, S. Y. Kim, J. H. Song, Y.-G. Lee, S.-Y. Lee, Y. S. Jung, *Nano Lett.* **2015**, *15*, 3317-3323.

[149]   C. Wang, X.-W. Zhang, A. J. Appleby, *J. Electrochem. Soc.* **2005**, *152*, A205-A209.

[150]   Q. Zhang, D. Cao, Y. Ma, A. Natan, P. Aurora, H. Zhu, *Adv. Mater.* **2019**, *31*, 1901131.

[151]   Y. Liu, P. He, H. Zhou, *Adv. Energy Mater.* **2018**, *8*, 1701602.

[152]   F. Zheng, M. Kotobuki, S. Song, M. O. Lai, L. Lu, *J. Power Sources* **2018**, *389*, 198-213.

[153]   T. Yang, Z. D. Gordon, Y. Li, C. K. Chan, *J. Phys. Chem. C* **2015**, *119*, 14947-14953.

[154]   T. Yang, J. Zheng, Q. Cheng, Y.-Y. Hu, C. K. Chan, *ACS Appl. Mater. Interfaces* **2017**, *9*, 21773-21780.

[155]   Z. Wan, D. Lei, W. Yang, C. Liu, K. Shi, X. Hao, L. Shen, W. Lv, B. Li, Q. H. Yang, *Adv. Funct. Mater.* **2019**, *29*, 1805301.

[156]   N. Kamaya, K. Homma, Y. Yamakawa, M. Hirayama, R. Kanno, M. Yonemura, T. Kamiyama, Y. Kato, S. Hama, K. Kawamoto, *Nat. Mater.* **2011**, *10*, 682-686.

[157]   Y. Seino, T. Ota, K. Takada, A. Hayashi, M. Tatsumisago, *Energy Environ. Sci.* **2014**, *7*, 627-631.

[158] Y.-Z. Sun, J.-Q. Huang, C.-Z. Zhao, Q. Zhang, *Science China Chemistry* **2017**, *60*, 1508-1526.

[159] A. Sakuda, A. Hayashi, M. Tatsumisago, *Sci. Rep.* **2013**, *3*, 2261.

[160] H. Sun, Y. Zhang, J. Zhang, X. Sun, H. Peng, *Nat. Rev. Mater.* **2017**, *2*, 1-12.

[161] W. Weng, Q. Sun, Y. Zhang, H. Lin, J. Ren, X. Lu, M. Wang, H. Peng, *Nano Lett.* **2014**, *14*, 3432-3438.

[162] Y. H. Kwon, S. W. Woo, H. R. Jung, H. K. Yu, K. Kim, B. H. Oh, S. Ahn, S. Y. Lee, S. W. Song, J. Cho, *Adv. Mater.* **2012**, *24*, 5192-5197.

[163] J. Park, M. Park, G. Nam, J. s. Lee, J. Cho, *Adv. Mater.* **2015**, *27*, 1396-1401.

[164] Y. Xu, Y. Zhao, J. Ren, Y. Zhang, H. Peng, *Angew. Chem. Int. Edit.* **2016**, *55*, 7979-7982.

[165] Z. Wang, Z. Ruan, Z. Liu, Y. Wang, Z. Tang, H. Li, M. Zhu, T. F. Hung, J. Liu, Z. Shi, *J. Mater. Chem. A* **2018**, *6*, 8549-8557.

[166] C. Song, Y. Li, H. Li, T. He, Q. Guan, J. Yang, X. Li, J. Cheng, B. Wang, *Nano Energy* **2019**, *60*, 285-293.

[167] A. M. Zamarayeva, A. E. Ostfeld, M. Wang, J. K. Duey, I. Deckman, B. P. Lechêne, G. Davies, D. A. Steingart, A. C. Arias, *Sci. Adv.* **2017**, *3*, e1602051.

[168] W. G. Chong, J. Q. Huang, Z. L. Xu, X. Qin, X. Wang, J. K. Kim, *Adv. Funct. Mater.* **2017**, *27*, 1604815.

[169] J. Cao, C. Chen, Q. Zhao, N. Zhang, Q. Lu, X. Wang, Z. Niu, J. Chen, *Adv. Mater.* **2016**, *28*, 9629-9636.

[170] H. Wang, W. Zhang, H. Liu, Z. Guo, *Angew. Chem. Int. Edit.* **2016**, *55*, 3992-3996.

[171] P. Zhu, C. Yan, J. Zhu, J. Zang, Y. Li, H. Jia, X. Dong, Z. Du, C. Zhang, N. Wu, *Energy Storage Mater.* **2019**, *17*, 220-225.

[172]   J. Wang, G. Yang, J. Chen, Y. Liu, Y. Wang, C. Y. Lao, K. Xi, D. Yang, C. J. Harris, W. Yan, *Adv. Energy Mater.* **2019**, *9*, 1902001.

[173]   L. Li, Z. P. Wu, H. Sun, D. Chen, J. Gao, S. Suresh, P. Chow, C. V. Singh, N. Koratkar, *ACS Nano* **2015**, *9*, 11342-11350.

[174]   Y. Liang, C. Z. Zhao, H. Yuan, Y. Chen, W. Zhang, J. Q. Huang, D. Yu, Y. Liu, M. M. Titirici, Y. L. Chueh, *InfoMat* **2019**, *1*, 6-32.

[175]   G. Qian, X. Liao, Y. Zhu, F. Pan, X. Chen, Y. Yang, *ACS Energy Lett.* **2019**, *4*, 690-701.

[176]   M. Li, W. Wahyudi, P. Kumar, F. Wu, X. Yang, H. Li, L.-J. Li, J. Ming, *ACS Appl. Mater. Interfaces* **2017**, *9*, 8047-8054.

[177]   B. Zheng, N. Li, J. Yang, J. Xi, *Chem. Comm.* **2019**, *55*, 2289-2292.

[178]   J. Wang, Y. Yang, F. Kang, *Electrochim. Acta* **2015**, *168*, 271-276.

[179]   D. K. Lee, C. W. Ahn, H.-J. Jeon, *J. Power Sources* **2017**, *360*, 559-568.

[180]   Y. Yang, W. Sun, J. Zhang, X. Yue, Z. Wang, K. Sun, *Electrochim. Acta* **2016**, *209*, 691-699.

[181]   D. K. Lee, S. J. Kim, Y. J. Kim, H. Choi, D. W. Kim, H. J. Jeon, C. W. Ahn, J. W. Lee, H. T. Jung, *Advanced Materials Interfaces* **2019**, *6*, 1801992.

[182]   M. Chen, C. Li, X. Fu, W. Wei, X. Fan, A. Hattori, Z. Chen, J. Liu, W. H. Zhong, *Adv. Energy Mater.* **2020**, *10*, 1903642.

[183]   S. Li, G. Ren, M. N. F. Hoque, Z. Dong, J. Warzywoda, Z. Fan, *Appl. Surf. Sci.* **2017**, *396*, 637-643.

[184]   L. Li, L. Hou, J. Cheng, T. Simmons, F. Zhang, L. T. Zhang, R. J. Linhardt, N. Koratkar, *Energy Storage Mater.* **2018**, *15*, 388-395.

[185]   J. H. Kim, J. Seo, J. Choi, D. Shin, M. Carter, Y. Jeon, C. Wang, L. Hu, U. Paik, *ACS Appl. Mater. Interfaces* **2016**, *8*, 20092-20099.

[186]   W. Kong, D. Wang, L. Yan, Y. Luo, K. Jiang, Q. Li, L. Zhang, S. Lu, S. Fan, J. Li, *Carbon* **2018**, *139*, 896-905.

[187]   Y. Guo, G. Zhao, N. Wu, Y. Zhang, M. Xiang, B. Wang, H. Liu, H. Wu, *ACS Appl. Mater. Interfaces* **2016**, *8*, 34185-34193.
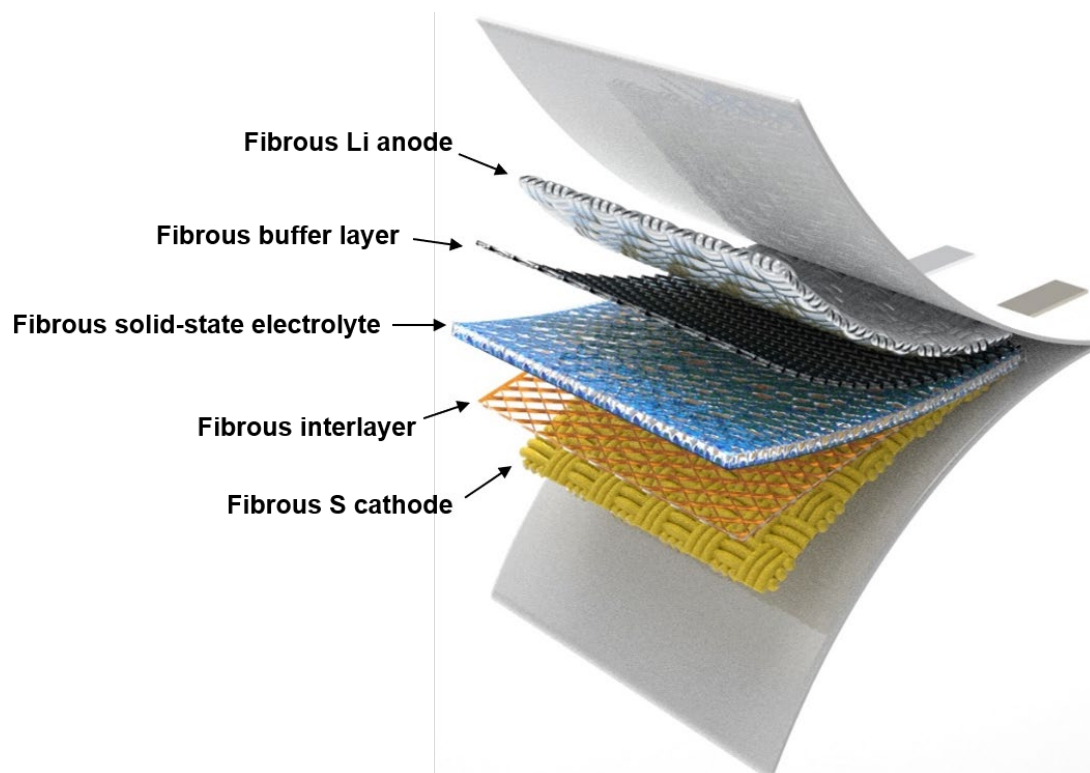
Figure 1. The schematic image depicts the flexible Li-S batteries fabricated with fibrous materials. Fibrous materials can work as flexible current collectors of Li anode and S cathode, and flexible interfacial layers (*e.g.* buffer layers, interlayers, and SSEs) in a flexible Li-S battery.
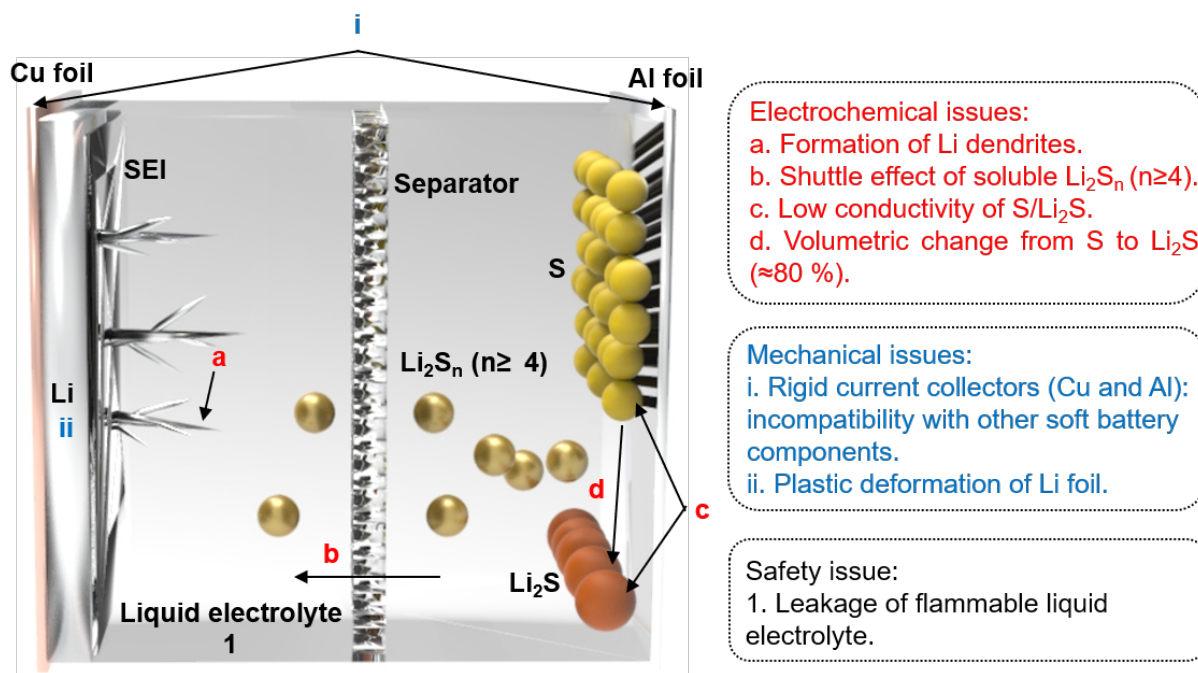
Figure 2. The schematic image illustrates the challenges of Li-S batteries, which includes electrochemical issues, mechancial issues, and safety issue.
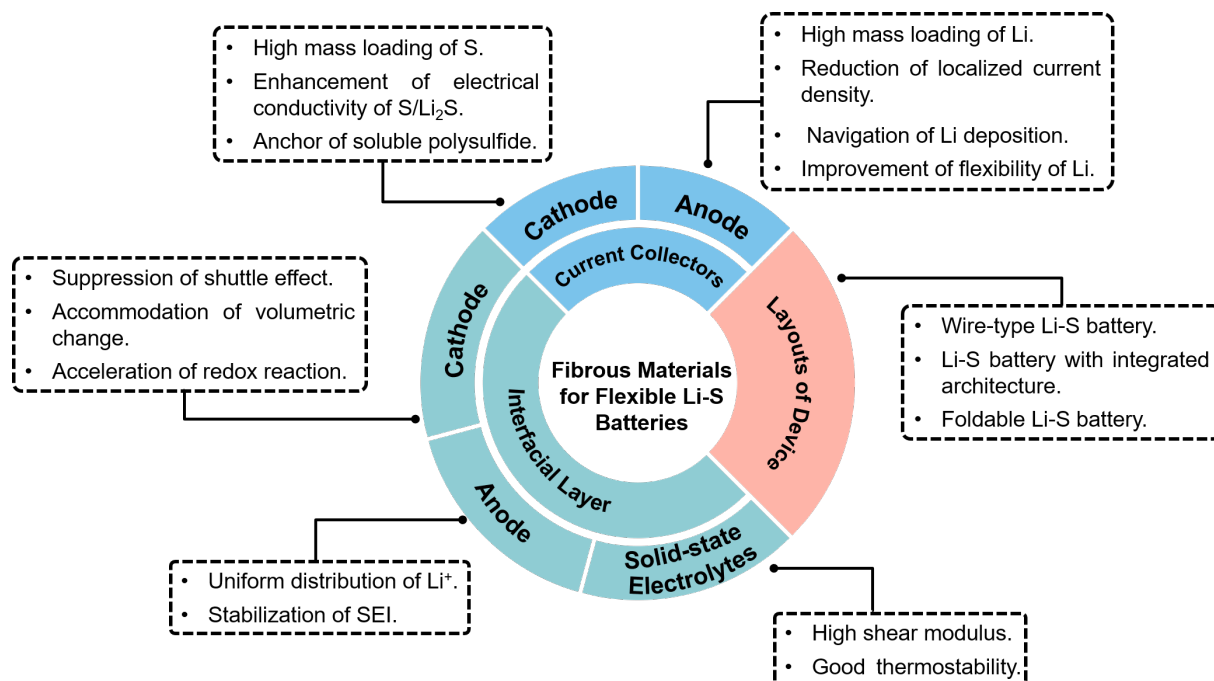
Figure 3. The advantages of fibrous material applications in flexible Li-S batteries.
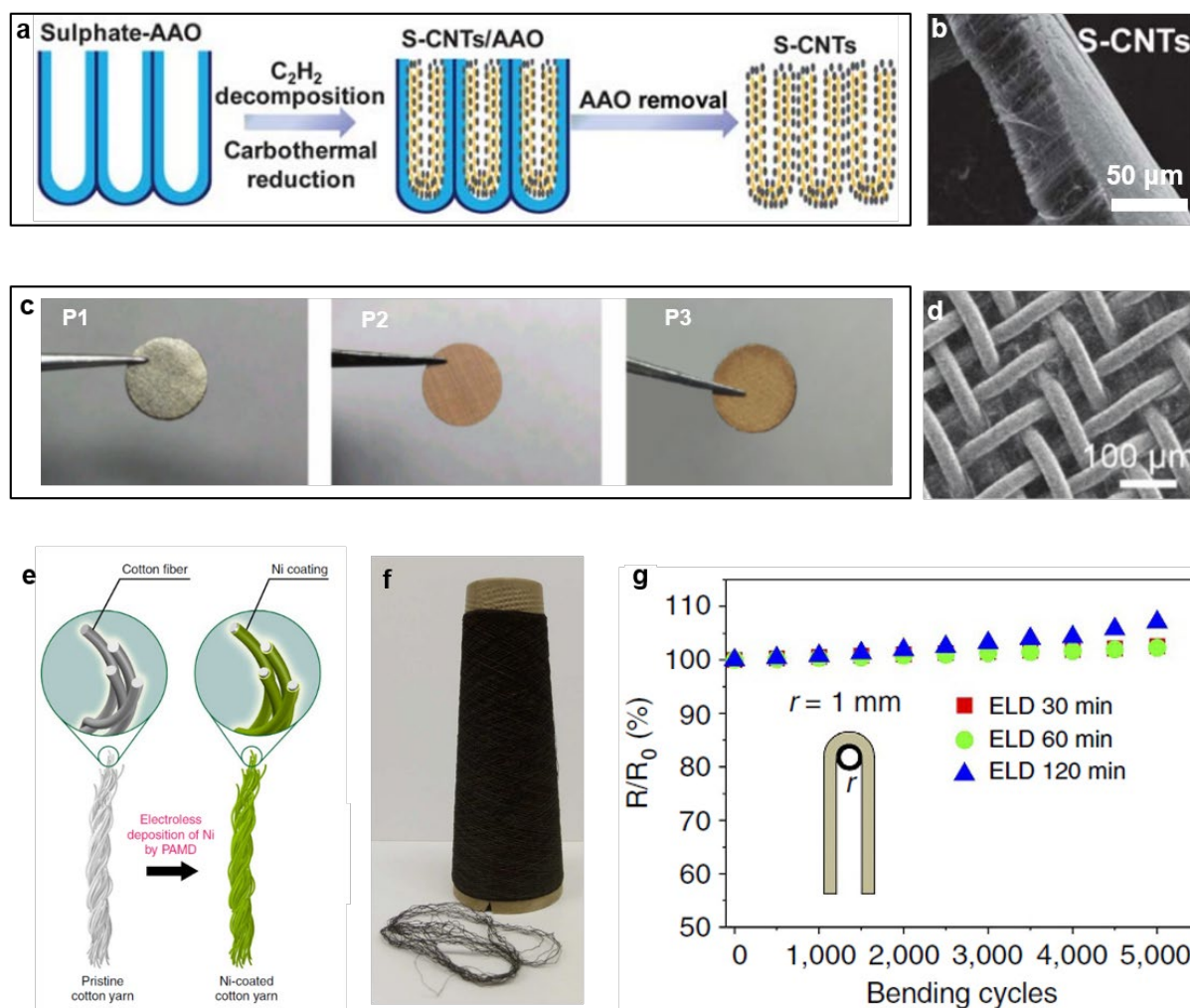
Figure 4. a) The schematic image exhibits the CVD-grown S-CNT electrode. b) The SEM image of as-fabricated S-CNT electrode. Reprinted with permission.[55] Copyright 2012, The Royal Society of Chemistry. c) Optical images of Li foil (P1), Cu mesh (P2), and Li embedded Cu mesh by pressing Li foil into the Cu mesh (P3). d) The SEM image of Li embedded Cu mesh. Reprinted with permission.[24] Copyright 2017, WILEY Verlag GmbH & Co. KGaA, Weinheim. e) The schematic image shows the deposition of Ni on the fibrous substrates via the method of PAMD. f) Digital image of a 500 m Ni-coated cotton yarn wound on a spinning cone. g) The electrical resistance of Ni-coated cotton yarns with different deposition times bent at a radius of 1 mm. Reprinted with permission.[21] Copyright 2015, Springer Nature.
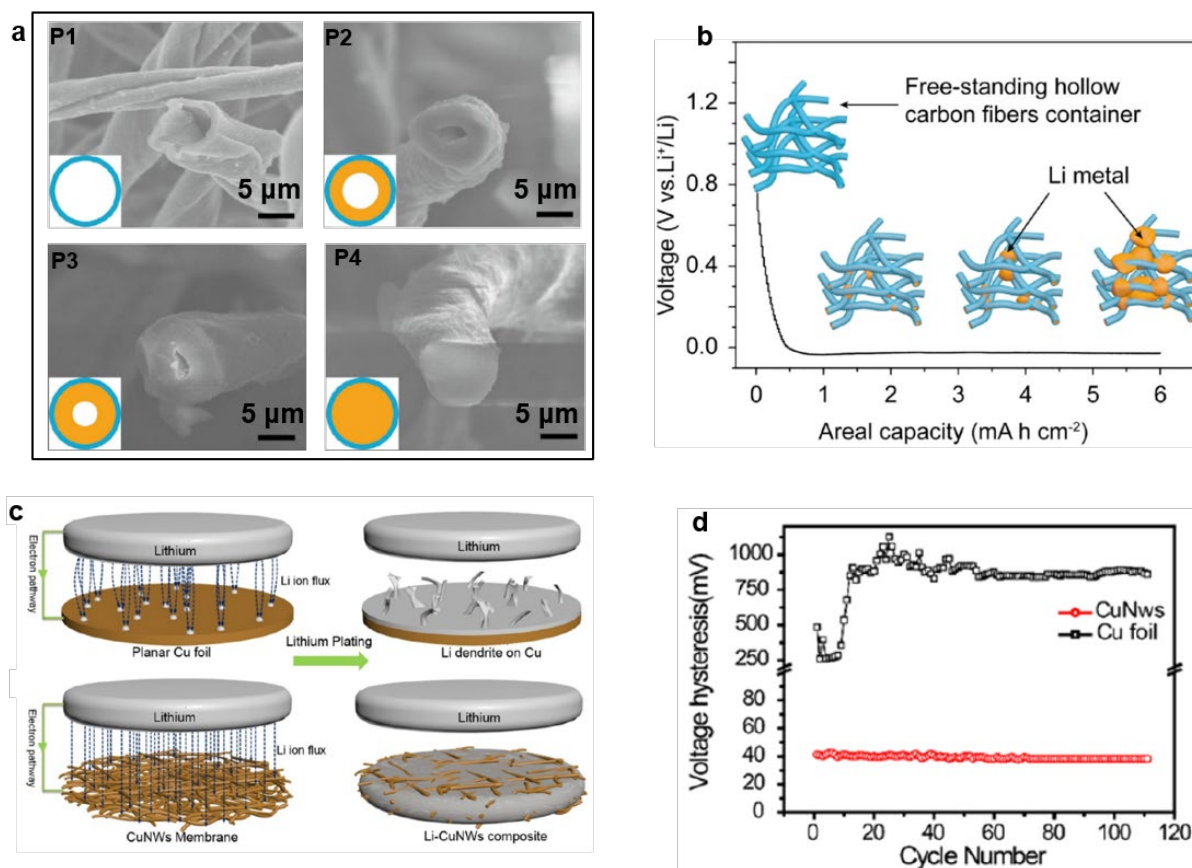
Figure 5. a) SEM images of the morphological change in a single hollow CNF with the increase of Li deposition. b) The schematic diagram shows the behavior of Li deposition on the flexible 3D-HCNF host. The Li firstly deposits inside the hollow CNF, then the interspace between neighboring CNFs. Reprinted with permission.[63] Copyright 2017, Elsevier Inc. c) The schematic illustration indicates the suppression of Li dendrites by replacing the Cu foil with Cu nanowires. d) The voltage hysteresis of Li deposition on the Cu foil and Cu nanowires. Reprinted with permission.[69] Copyright 2016, American Chemical Society.
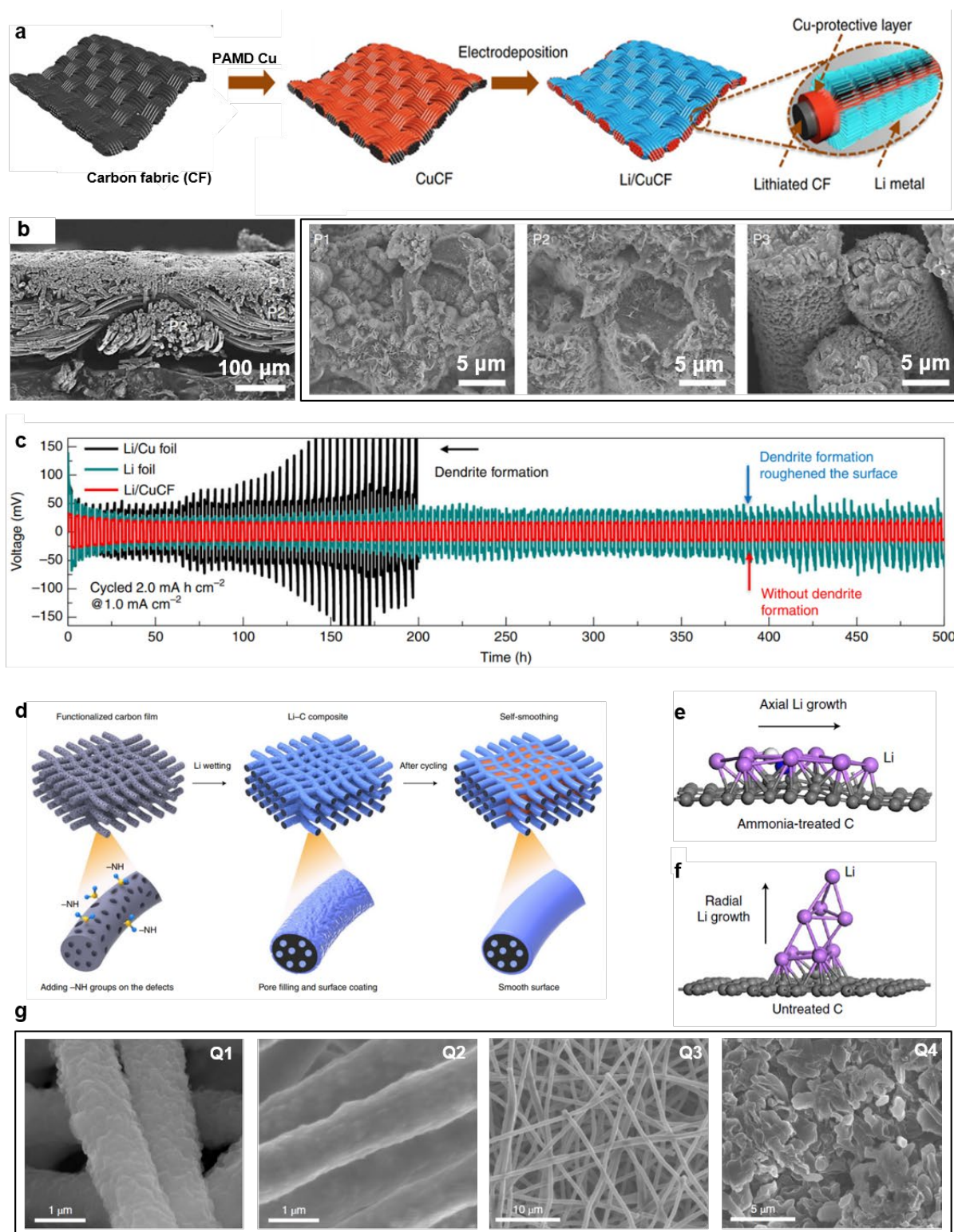
Figure 6. a) The schematic image shows the fabrication of fibrous Li anode via the electrochemical deposition of Li on the CuCF. b) SEM images of as-fabricated fibrous Li anode, where P1, P2, P3 show the morphologies at different positions of fibrous Li anode. The results

indicate the uniform and conformal coating of Li nanoflakes on the surface of CuCF. c) The long-term cycling tests of Li/Cu foil, Li foil, and Li/CuCF symmetric cells at 1 mA cm^{-2}. Reprinted with permission.[74] Copyright 2018, Springer Nature. d) The schematic image illustrates the fabrication of fibrous Li via the infusion of molten Li into functionalized CFs. e, f) The DFT calculation of Li growth on the ammonia-treated and non-treated CFs. The colors of grey, blue, white and purple refer to the atoms of C, N, H, and Li, respectively. g) SEM images of ammonia-treated CFs after infusion of molten Li before cycling test (Q1) and after 200 cycles' test (Q2, Q3). The smooth surface after cycling test results from the navigation of Li deposition by the functional groups. P4 is the SEM image of a Li foil after 10 cycles' test. The uneven deposition of Li roughens the surface of Li foil. Reprinted with permission.[75] Copyright 2019, Springer Nature.
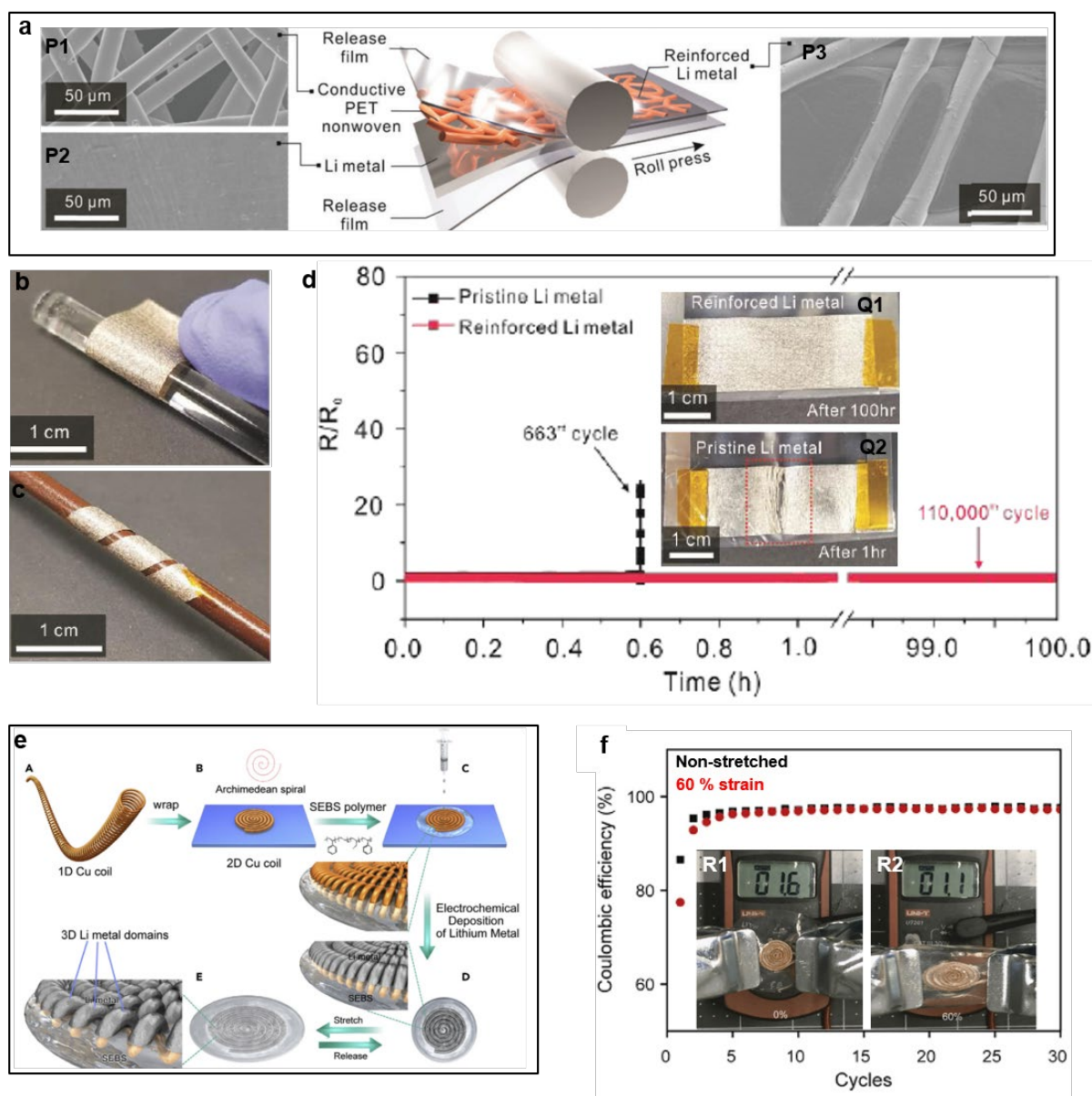
Figure 7. a) The schematic image shows the fabrication of reinforced Li anode by rolling press. Inset shows the SEM images of conductive PET (P1), pristine Li foil (P2), and reinforced Li anode (P3). b, c) Digital images of flexible reinforced Li anode. d) Mechanical durability of reinforced Li anode and pristine Li foil. Inset shows the digital images of reinforced Li metal (Q1) and prisitine Li metal (Q2) after flexing test. Reprinted with permission.[42] Copyright 2019, The Royal Society of Chemistry. e) The schematic image shows the fabrication of stretchable Li anode. f) Cycling performances of Li anode tested at non-stretched (R1) and 60 % strain (R2). Reprinted with permission.[31] Copyright 2018, Elsevier Inc.
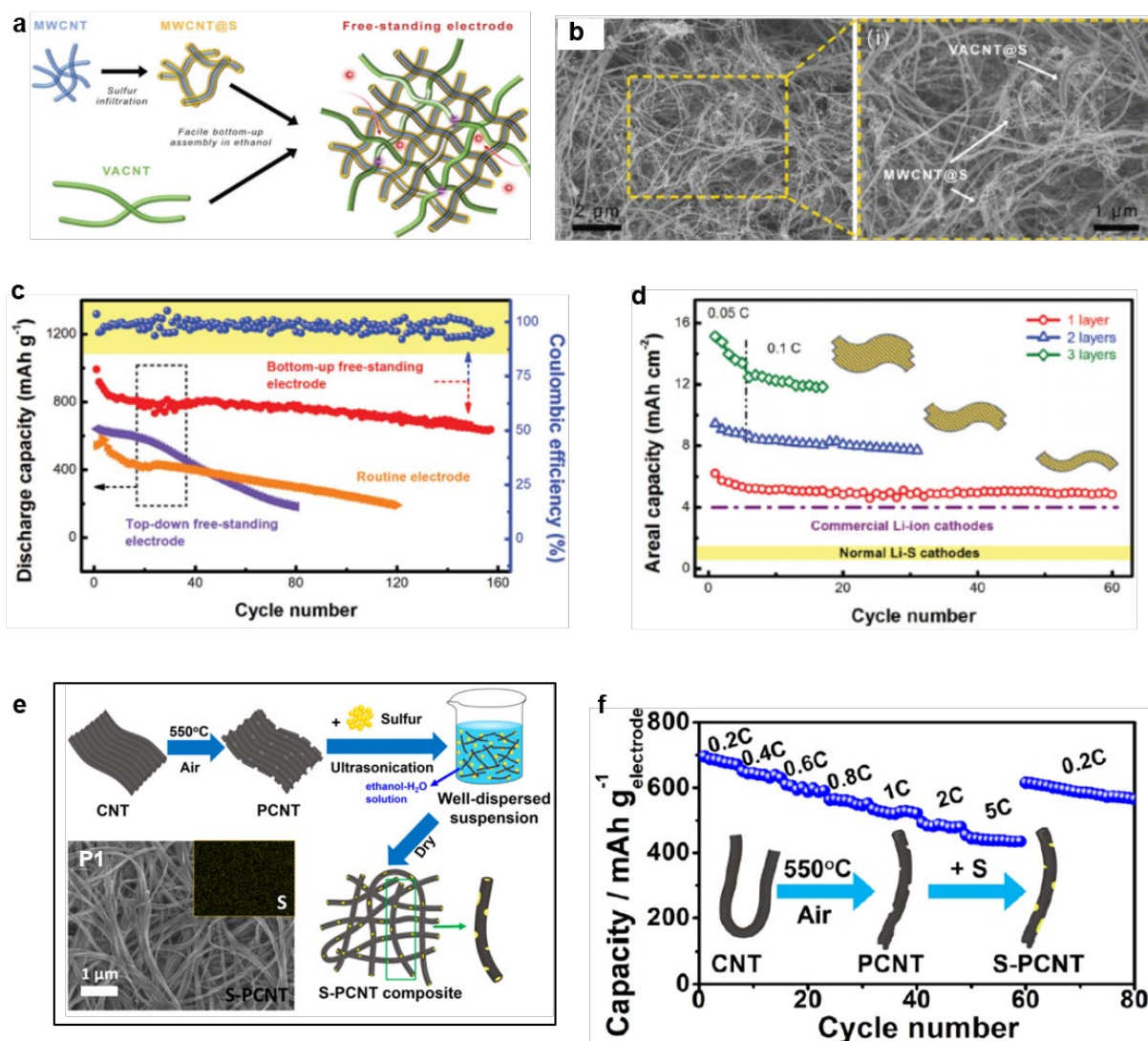
Figure 8. a) The schematic image shows the fabrication of hierarchical CNT-based S cathode. b) The SEM image of as-fabricated hierarchical CNT-based S cathode. c) Cycling performances of hierarchical CNT-based S cathode and conventional S cathode. d) Cycling performances of high areal capacities with stacked electrodes. Reprinted with permission.[86] Copyright 2014, WILEY-VCH Verlag GmbH & Co. KGaA, Weinheim. e) The schematic image shows the fabrication process of mesoporous SACNTs-based S cathode. Inset (P1) shows the SEM image of as-fabricated S cathode. f) Rate capability of mesoporous SACNTs-based S cathode. Reprinted with permission.[91] Copyright 2016, American Chemical Society.
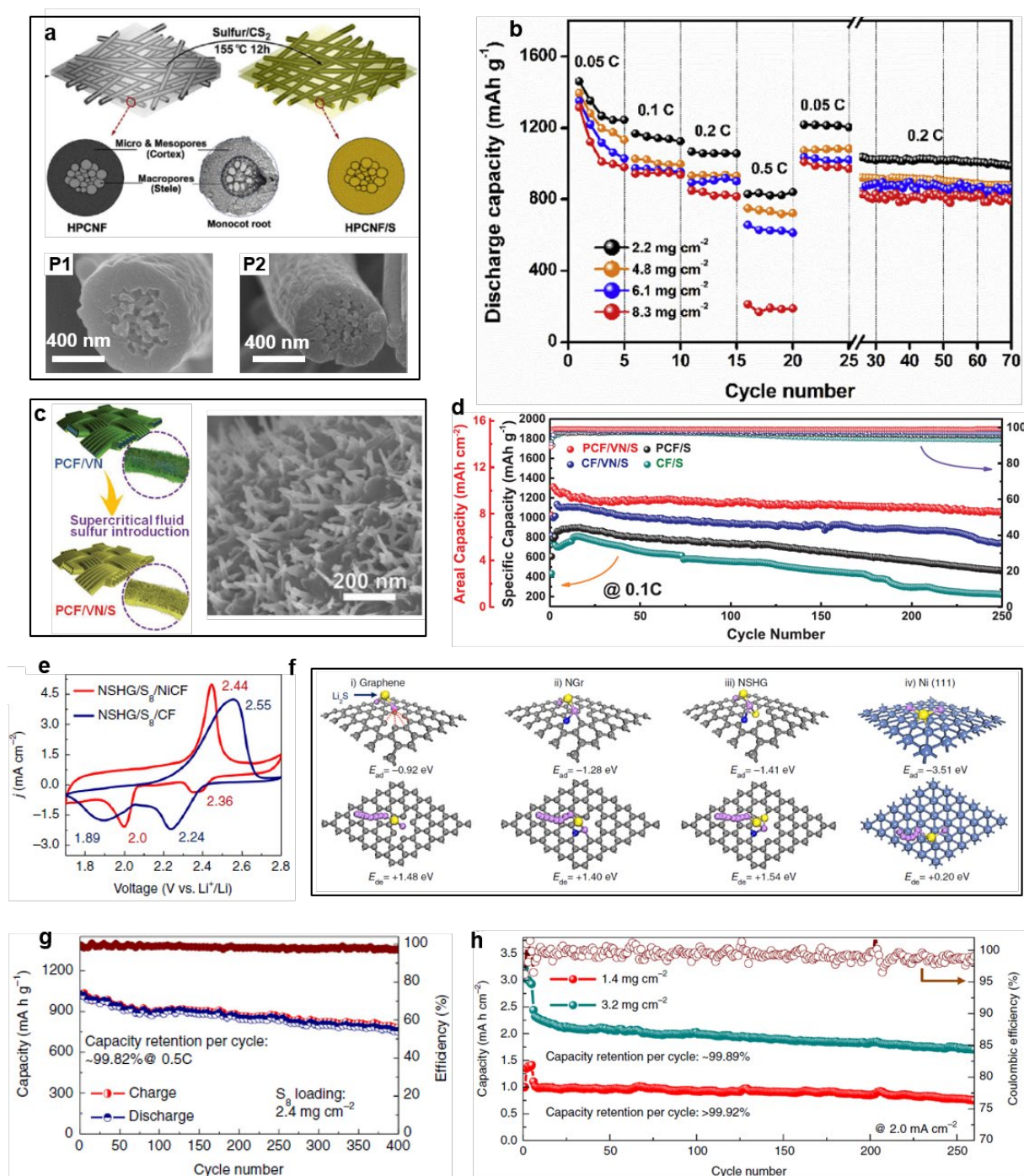
Figure 9. a) The schematic illustration of the fabrication of HPCNF-based current collector (P1) and S @HPCNF cathode (P2). b) The rate capability of Li-S batteries fabricated with S @HPCNF cathode with different mass loading. Reprinted with permission.[95] Copyright 2017, Elsevier. c) The schematic and SEM images of PCF/VN/S. d) Cycling performances of PCF/VN/S, CF/VN/S, PCF/S and CF/S electrodes @0.1 C. Reprinted with permission.[110]

Copyright 2018, WILEY-VCH Verlag GmbH & Co. KGaA, Weinheim. e) The cyclic voltammetry curves of NSHG/S/NiCF and NSHG/S/CF at the scan rate of 0.2 mV s^{-1}. The result indicates the catalytic function of Ni. f) The DFT calculation of the adsorption and decomposition energies of Li$_2$S on the surface of rGO, NGr, NSHG, and Ni (111). The colors of gray, yellow, purple, blue, and light blue refer to the atoms of C, S, Li, N, and Ni. g) The cycling performance of NSHG/S/NiCF cathode with a loading of S of 2.4 mg cm^{-2} tested @0.5 C. h) The cycling stability of the Li-S batteries fabricated with NSHG/S/NiCF cathode (the loading of S are 1.4 mg cm^{-2} and 3.2 mg cm^{-2}, respectively) and Li anode (6 mAh cm^{-2}) tested at different current densities. Reprinted with permission.[74] Copyright 2018, Springer Nature.
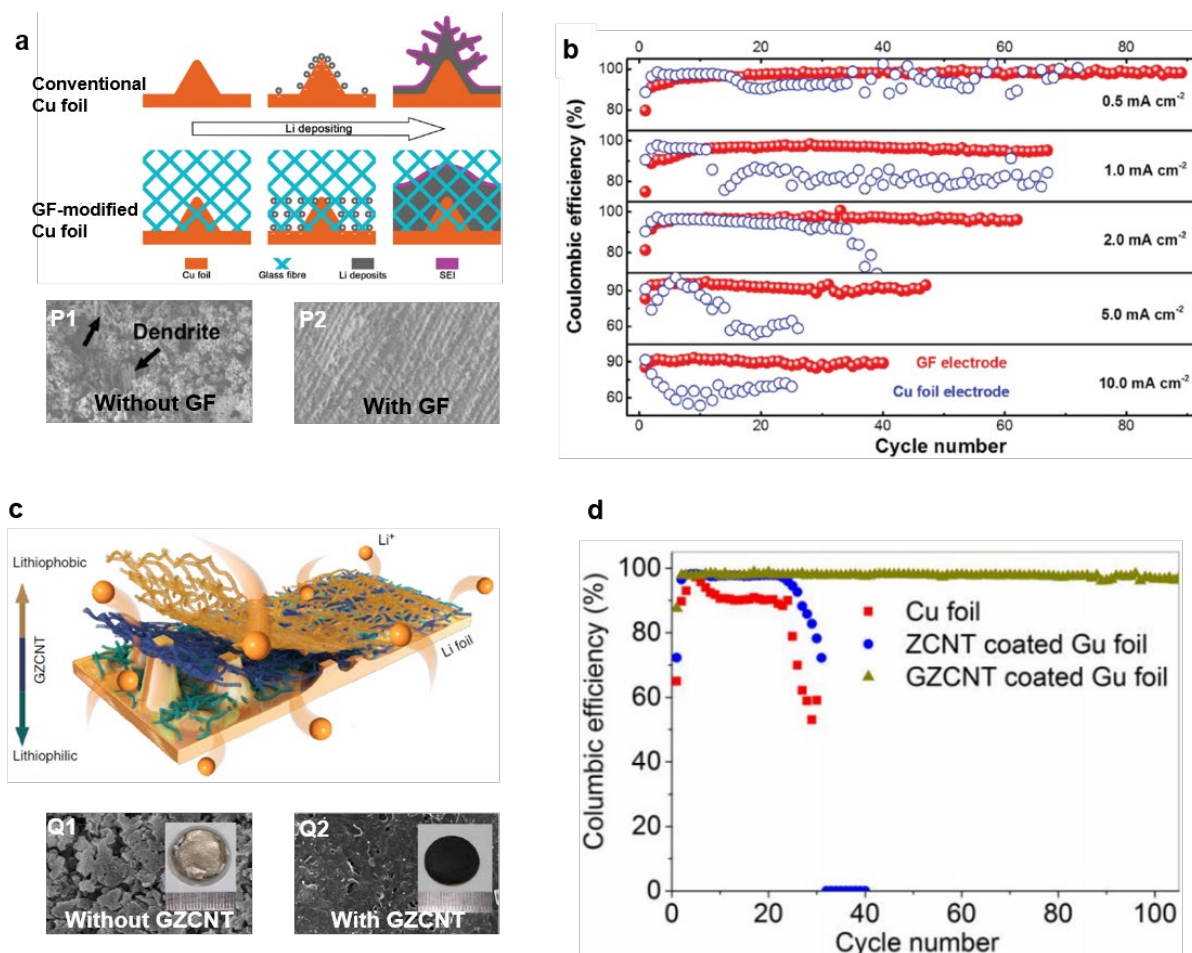
Figure 10. a) The schematic image illustrates the suppression of the growth of Li dendrites by adding a GF buffer layer. SEM results show the morphologies of as-deposited Li without (P1) and with using a buffer layer (P2). b) The CE of bare Cu foil and GF-modified Cu foil at different current densities. Reprinted with permission.[131] Copyright 2016, WILEY-VCH Verlag GmbH & Co. KGaA, Weinheim. c) The schematic image of a buffer layer with lithiophilic-lithiophobic gradient. SEM and digital images show the blank Li anode (Q1), where the anode surface is buried under the mossy Li deposits, and buffer layer coated Li anode (Q2) after 200 cycles' test. d) The CE of bare Cu foil, buffer layer coated Cu foil (without lithiophilic gradient), and buffer layer coated Cu foil (with lithiophilic gradient) at a current density of 2.0 mA cm^{-2}. Reprinted with permission.[132] Copyright 2018, Springer Nature.
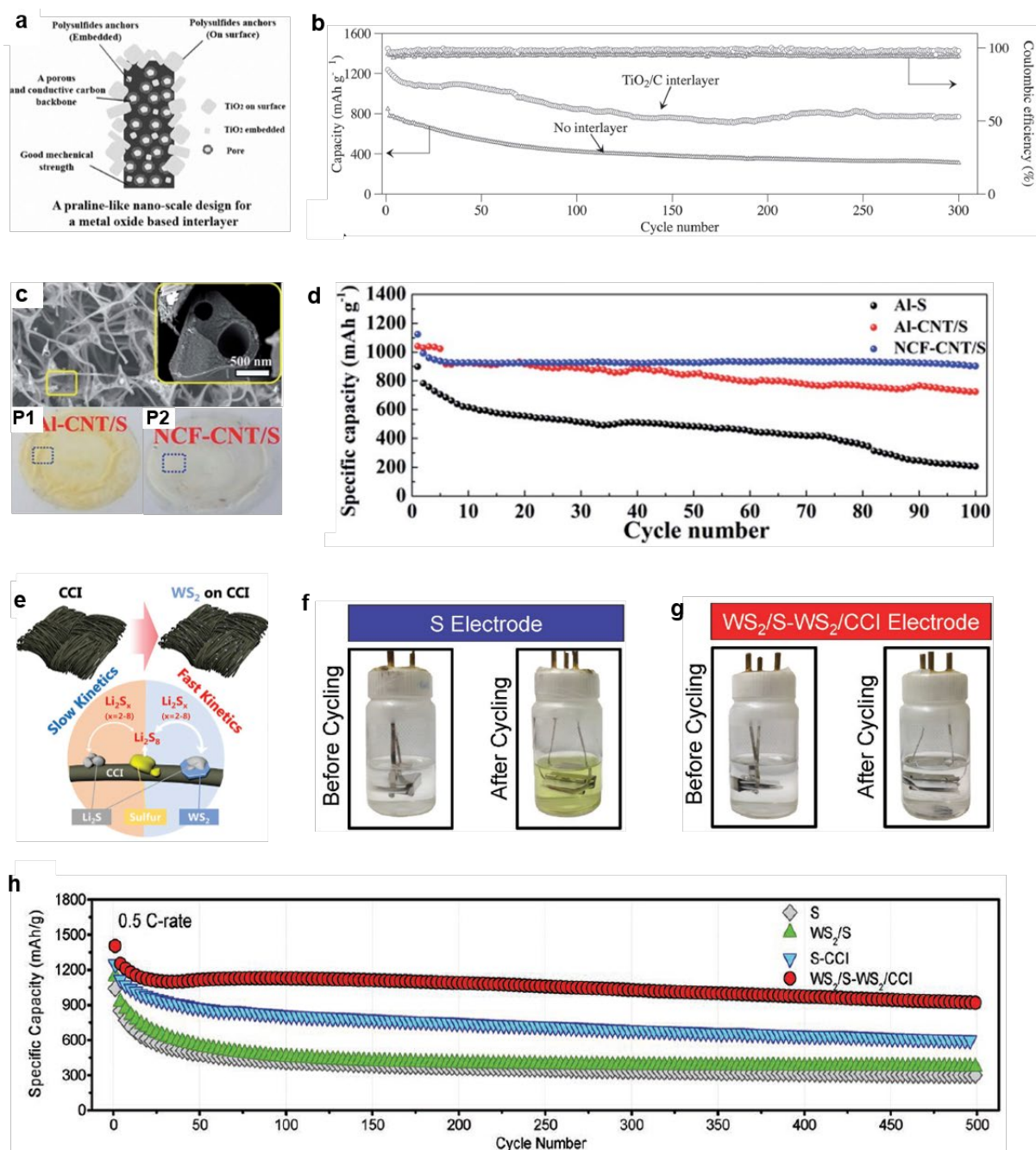
Figure 11. a) The schematic image illustrates the advantages of flexible TiO₂/C interlayer. b) Cycling performance of the S cathodes with and without the TiO₂/C interlayer tested @0.2 C. Reprinted with permission.[135] Copyright 2017, WILEY-VCH Verlag GmbH & Co. KGaA, Weinheim. c) SEM images of the elastic interlayer made with NCF-CNT. Optical images of the S cathodes without (P1) and with elastic interlayer (P2) after cycling for 100 cycles. d) Cycling performances of NCF-CNT/S cathode, Al-CNT/S cathode and traditional Al-S cathode

tested @0.5 C. Reprinted with permission.[94] Copyright 2016, The Royal Society of Chemistry. e) The schematic image illustrates the fast kinetics of WS_2 supported carbon cloth. f, g) Digital images show the vial cells with bare S cathode and interlayer coated S cathode. The occurrence of the yellowish color in the via cell with bare S cathode indicates the dissolution of soluble polysulfides into the electrolyte. h) Long-term cycling performances of S cathodes with and without interlayer tested @0.5 C. Reprinted with permission.[142] Copyright 2017, WILEY-VCH Verlag GmbH & Co. KGaA, Weinheim.
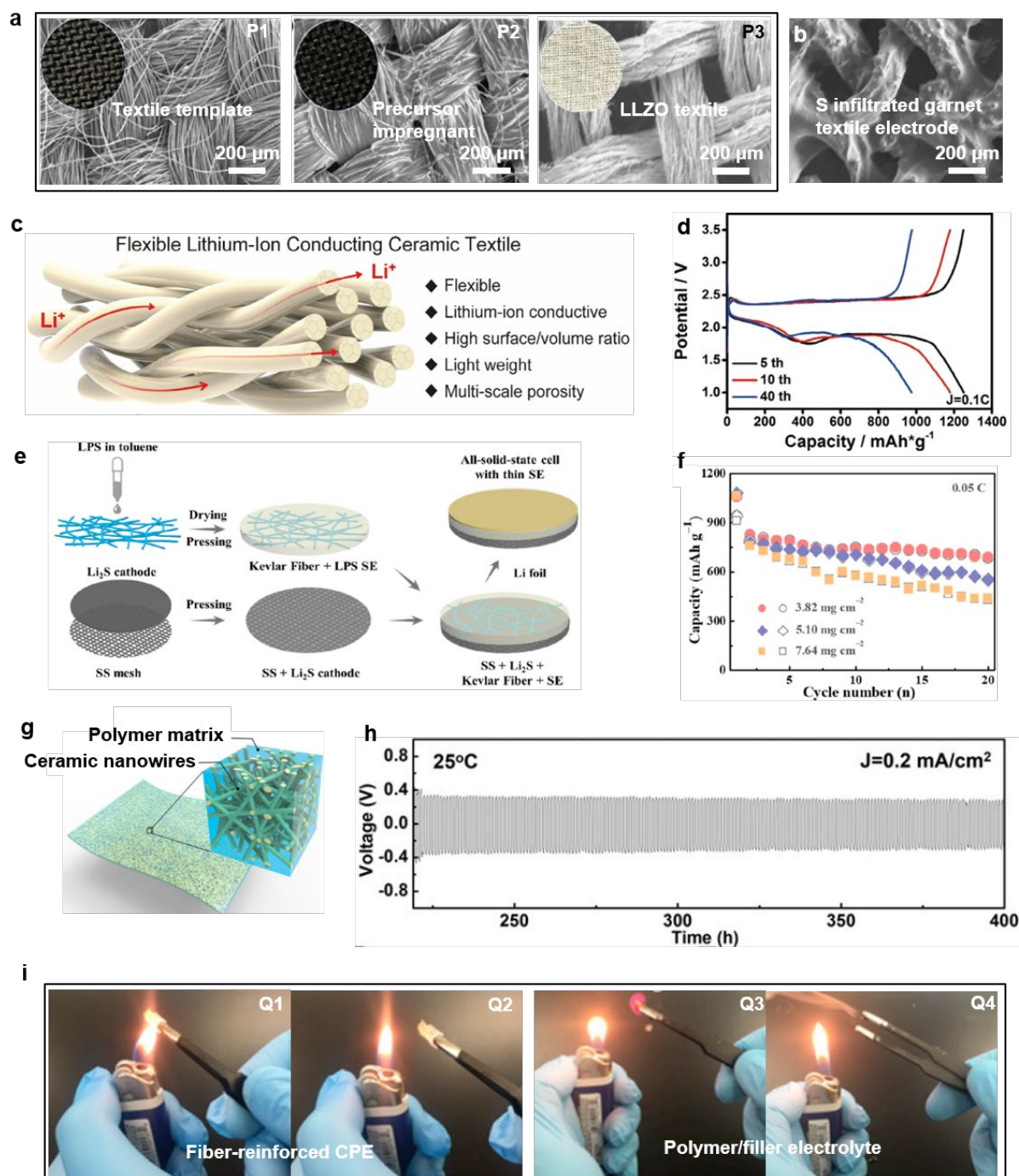
Figure 12. a) The digital and SEM images show the textile template (P1), textile template after precursor impregnant (P2), and as-fabricated LLZO textile (P3). b) The SEM image of flexible LLZO textile after infiltration of S with a mass loading of 10.8 mg cm^{-2}. c) The schematic image illustrates the advantages of as-fabricated LLZO textile. d) The voltage profile of solid-state Li-S battery fabricated with the LLZO textile. Reprinted with permission.[146] Copyright 2018, Elsevier Ltd. e) The schematic illustration of the fabrication process of solid-state Li-Li2S

battery with Kevlar nonwoven-reinforced sulfide solid electrolyte. f) Cycling performance of solid-state Li-Li$_2$S battery with different amounts of Li$_2$S @0.05 C. Reprinted with permission.[144] Copyright 2019, American Chemical Society. g) The schematic image of LLZO nanowire-based composite polymer electrolyte. h) The cyling stability of Li symmetric cell fabricated with LLZO nanowire-based composite polymer electrolyte. i) Flammability tests of LLZO nanowire-based composite polymer electrolyte (Q1, Q2) and conventional polymer/filler electrolyte (Q3, Q4). Reprinted with permission.[147] Copyright 2016, National Academy of Sciences.
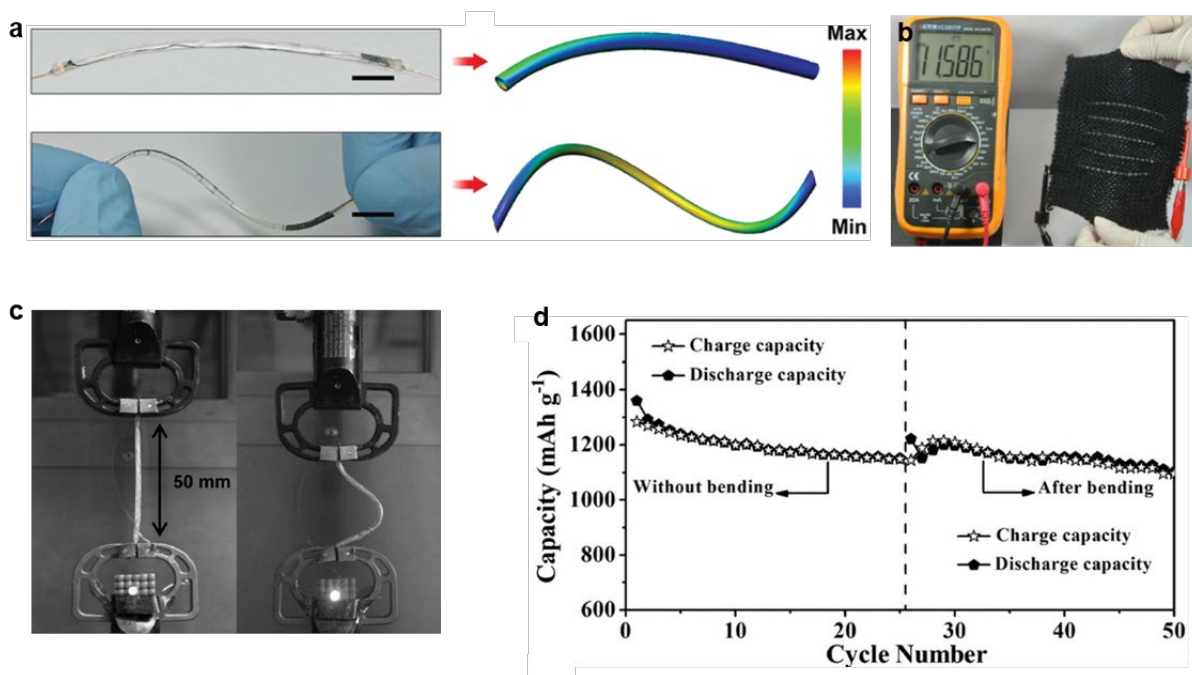
Figure 13. a) A wire-type Li-S battery and its stress distribution under bending and twisting states. The battery shows a uniform distribution of the stress. b) Wire-type Li-S batteries woven into the textile. Reprinted with permission.[88] Copyright 2015, WILEY-VCH Verlag GmbH & Co. KGaA, Weinheim. c) A wire-type Li-S battery with rGO/CNT/S cathode powering an LED subjected to bending in compression. Reprinted with permission.[168] Copyright 2016, WILEY-VCH Verlag GmbH & Co. KGaA, Weinheim. d) Cycling performance of a wire-type Li-S battery fabricated with rGO/S cathode before and after bending recorded @0.1 C. Reprinted with permission.[169] Copyright 2016, WILEY-VCH Verlag GmbH & Co. KGaA, Weinheim.
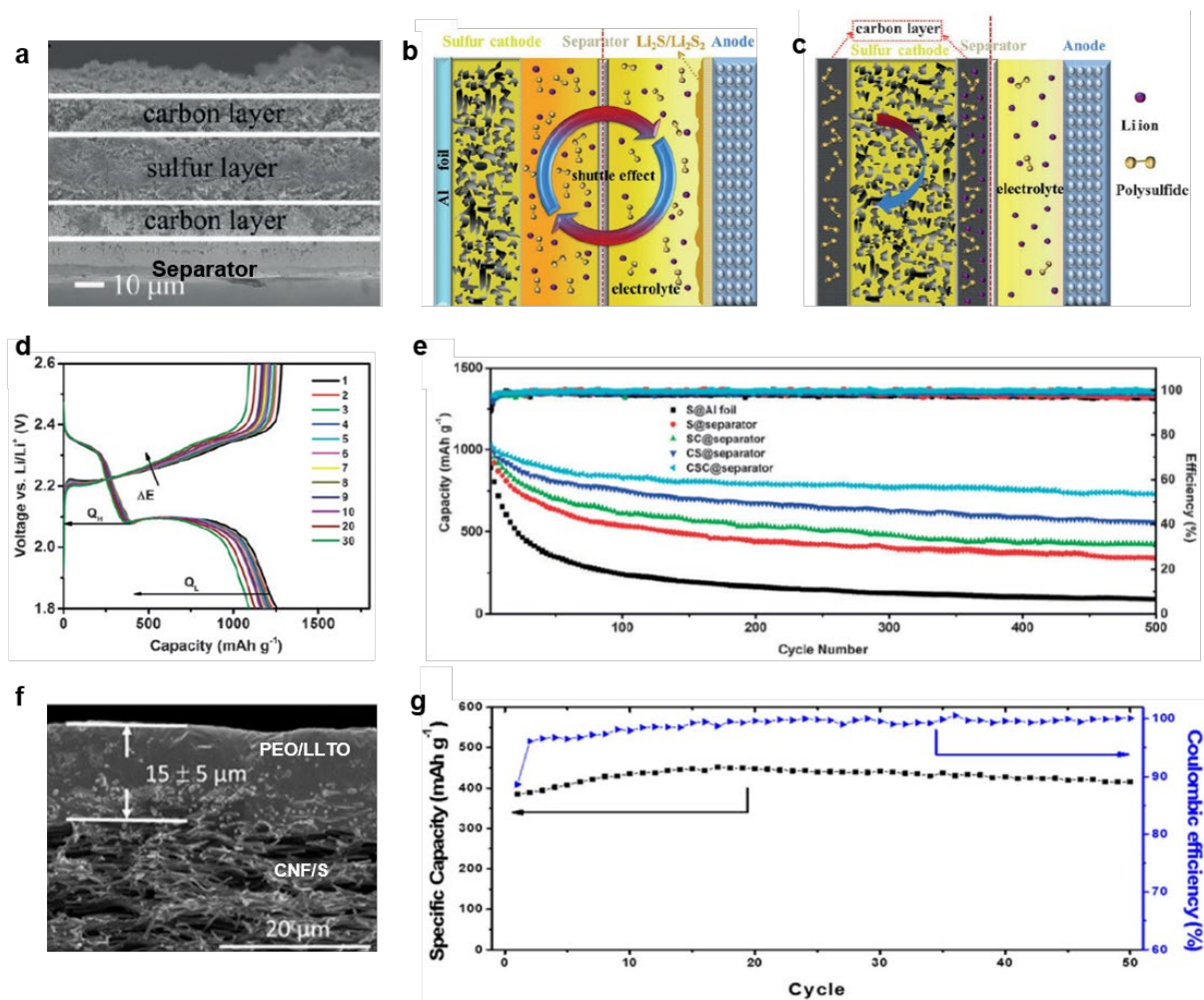
Figure 14. a) The SEM image of CSC @separator. b, c) The schematic images illustrate the advantages of using CSC @separator cathode over S @Al foil cathode. d) The voltage profiles of CSC @separator cathode. e) Long-term cycling performances of flexible Li-S batteries with S @Al foil cathode, CSC @separator cathode, and a series of integrated cathodes tested @0.6 C. Reprinted with permission.[170] Copyright 2016, WILEY-VCH Verlag GmbH & Co. KGaA, Weinheim. f) The SEM image shows the CNF/S-PEO/LLTO bilayer framework. g) The cycling performance of the solid-state Li-S battery assembled with CNF/S-PEO/LLTO electrode tested @0.05 C with a S loading of 1.27mg cm^{-2}. Reprinted with permission.[171] Copyright 2018, Elsevier.
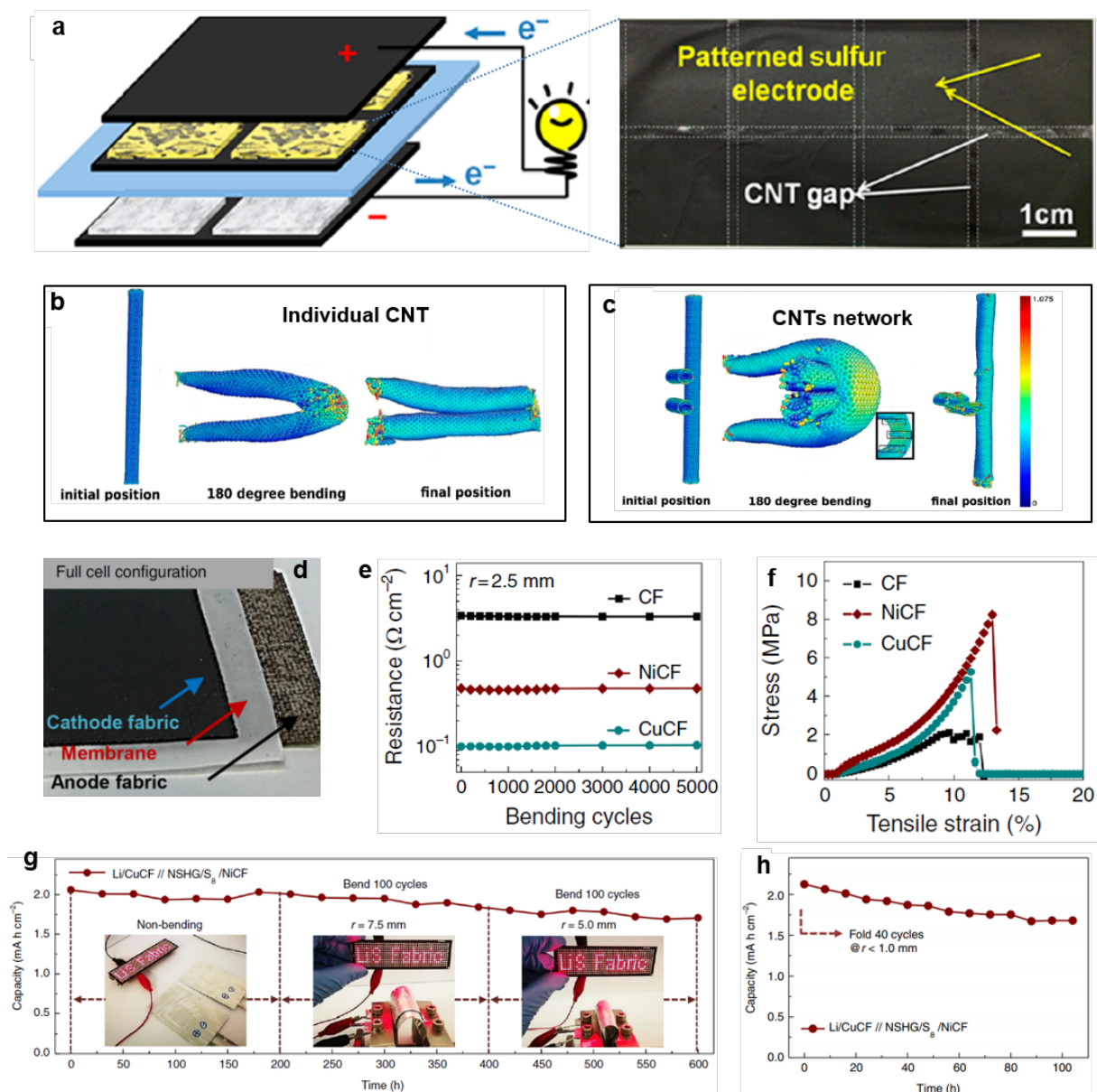
Figure 15. a) A foldable Li-S battery with a checkboard pattern. b, c) The MD simulation of the stress distribution of individual CNT and CNTs network under folding condition. The results indicate the CNTs network can withstand higher stress than that of individual CNT under the folding condition without significant plastic deformation. Reprinted with permission.[173] Copyright 2015, American Chemical Society. d) The digital image of the fabric-type Li-S battery. e) The sheet resistance of CF, CuCF, NiCF as the function of bending cycles at a bending radius of 2.5 mm. f) The tensile stress-strain curves of CF, CuCF, and NiCF. g) The areal capacity of the fabric-type Li-S battery recorded during repeated bents at various radii.

Inset shows the digital images of two seriesly connected fabric-type Li-S batteries powering an LED pannel. h) The areal capacity of fabric-type Li-S battery tested during 40 repeated folds. Reprinted with permission.[74] Copyright 2018, Springer Nature.

Table 1. Summary of the functions of interlayers and correlated enhancements of battery performances

Materials	Structural properties	Functions	C1	C2	S loading	Battery CE
CNT/cellulose paper[176]	NA	S-function (physical immobilization) &K-function	556 mAh g^{-1} @0.25 C 0.664 % for 100 cycles	92 mAh g^{-1} @0.25 C 0.831 % for 100 cycles	0.974 mg cm^{-2}	≈98 %
Carbonized cotton cloth[177]	Mesopores (<5 nm)		610 mAh g^{-1} @0.5 C 0.076 % for 500 cycles	371 mAh g^{-1} @0.5 C 0.088 % for 500 cycles	1.0 mg cm^{-2}	NA
Activated CNF[178]	Hierarchical pores (0.9-2 nm, 2.5-10 nm)		897 mAh g^{-1} @0.1 C 0.27 % for 100 cycles	46 mAh g^{-1} @0.1 C 0.962% for 100 cycles	2.5 mg cm^{-2}	89 %- 99.2 %.
Graphitic CNF felt[179]	NA		1004.62 mAh g^{-1} @0.2 C 0.215 % for 100 cycles	344.92 mAh g^{-1} @0.2 C 0.561% for 100 cycles	0.7 mg cm^{-2}	≈100 %
CNF cloth[180]	Hierarchical pores (1.4-10 nm)		920 mAh g^{-1} @1.0 C 0.14 % for 100 cycles	182 mAh g^{-1} @1.0 C 0.643 % for 100 cycles	3.5 mg cm^{-2}	NA
CNT/GO[181]	Macropores		920 mAh g^{-1} @1.0 C 0.745 % for 100 cycles	520 mAh g^{-1} @0.2 C 1.133 % for 50 cycles	1.1 mg cm^{-2}	>99 %
CNF/MnS[72]	Mesopores (~2.89 nm)		810 mAh g^{-1} @1.0 C 0.05 % for 400 cycles	<250 mA h g^{-1} @1.0 C 400 cycles	2.0 mg cm^{-2}	NA
CNFs/gelatin[182]	NA		628 mAh g^{-1} @0.18 C 0.173 % for 250 cycles	384 mA h g^{-1} @0.18 C 0.287 % for 150 cycles	1.8 mg cm^{-2}	99.0%
Graphene-embedded CNF film[124]	Mesopores (≈40 nm)		698mAh g^{-1} @1.0 C 0.1472 % for 300 cycles	Rapid decay	1.2 mg cm^{-2}	≈100 %
Cellulose filter paper[183]	NA		830 mAh g^{-1} @0.2 C 0.105 % for 130 cycles	200 mAh g^{-1} @0.2 C 0.189 % for 130 cycles	1.39 mg cm^{-2}	>97 %

Material	Pore	Function	C1	C2	Loading	CE
MWCNTs/MnO$_2$[72]	NA		600 mAh g^{-1} @1 C 0.064 % for 500 cycles	225 mAh g^{-1} @1 C 0.073 % for 500 cycles	1.4 mg cm^{-2}	≈96 %
CNF/TiO$_2$ nanoparticles[135]	Mesopores (≈2.7 nm)		770.8 mAh g^{-1} @0.2C 0.127% for 300 cycles	420.5 mAh g^{-1} @0.2 C 0.168% for 300 cycles	3 mg cm^{-2}	≈99 %
CNF/Ti$_4$O$_7$[184]	Mesopores (2-16 nm)		945 mAh g^{-1} @0.2 C 0.275% for 100 cycles	415 mAh g^{-1} @0.2 C 0.599% for 100 cycles	NA	NA
Poly(acrylic acid) coated CNT[185]	NA		573 mAh g^{-1} @1 C 0.128% for 200 cycles	136 mAh g^{-1} @1 C 0.320% for 200 cycles	0.82 mg cm^{-2}	≈99%
Carbon cloth/WS$_2$[142]	NA		1000 mA h g^{-1} @0.5 C 0.055 % for 500 cycles	300 mA h g^{-1} @0.5 C 0.142 % for 500 cycles	3.0 mg cm^{-2}	NA
Graphene/V$_2$O$_5$ nanowire[134]	NA		516 mAh g^{-1} @0.5 C 0.042 % for 1000 cycles	Rapid decay over 100 cycles	1.5 mg cm^{-2}	>98 %
SACNTs/HfO$_2$[186]	NA		721 mAh g^{-1} @1 C 0.064 % for 500 cycles	600 mAh g^{-1} @1 C Failed after 280 cycles	1.80 mg cm^{-2}	≈98.4 %
Graphene nanoscroll[187]	Mesopores (≈3.2 nm)	S-function &K-function &V-function	744 mA h g^{-1} @1 C 100 cycles	199 mA h g^{-1} @1 C 100 cycles	NA	≈100%
TiO$_2$ embedded N-doping porous carbon[133]	Hierarchical pores (1.4-17 nm)		670 mAh g^{-1} @1 C 0.078 % for 300 cycles	< 300 mA h g^{-1} @1 C 100 cycles	1.4 mg cm^{-2}	≈100 %
N-doped carbon foam[94]	Hierarchical pores (<10 nm)		903 mA h g^{-1} @0.5 C 0.197 % for 100 cycles	724 mAh g^{-1} @0.5 C 0.769% for 100 cycles	1.2 mg cm^{-2}	98.6%

C1: Reversible capacity and performance decay per cycle with fibrous interlayer.

C2: Reversible capacity and performance decay per cycle without fibrous interlayer.

S-function: Suppression of shuttle effect.

K-function: Acceleration of reaction kinetics.

V-function: Accommodation of volumetric change.